

**The DESI Y1 RR Lyrae catalog II:  
The metallicity dependency of pulsational properties,  
the shape of the RR Lyrae instability strip, and metal rich RR Lyrae**

GUSTAVO E. MEDINA,<sup>1,2</sup> TING S. LI,<sup>1,2</sup> C. ALLENDE PRIETO,<sup>3,4</sup> L. BERALDO E SILVA,<sup>5,6</sup> A. BYSTRÖM,<sup>7</sup> R. G. CARLBERG,<sup>8</sup>  
S. E. KOPOSOV,<sup>7,9</sup> M. LAMBERT,<sup>10</sup> J. R. NAJITA,<sup>11</sup> C. ROCKOSI,<sup>12,13,14</sup> N. KIZHUPRAKKAT,<sup>15</sup> A. H. RILEY,<sup>16</sup> J. AGUILAR,<sup>17</sup>  
S. AHLEN,<sup>18</sup> D. BIANCHI,<sup>19,20</sup> D. BROOKS,<sup>21</sup> T. CLAYBAUGH,<sup>17</sup> A. P. COOPER,<sup>15</sup> A. DE LA MACORRA,<sup>22</sup> A. DEY,<sup>23</sup>  
P. DOEL,<sup>21</sup> J. E. FORERO-ROMERO,<sup>24,25</sup> E. GAZTAÑAGA,<sup>26,27,28</sup> S. GONTCHO A GONTCHO,<sup>17</sup> G. GUTIERREZ,<sup>29</sup> M. ISHAK,<sup>30</sup>  
R. KEHOE,<sup>31</sup> T. KISNER,<sup>17</sup> M. LANDRIAU,<sup>17</sup> L. LE GUILLOU,<sup>32</sup> A. MEISNER,<sup>23</sup> R. MIQUEL,<sup>33,34</sup> F. PRADA,<sup>35</sup>  
I. PÉREZ-RÀFOLS,<sup>36</sup> G. ROSSI,<sup>37</sup> E. SANCHEZ,<sup>38</sup> D. SCHLEGEL,<sup>17</sup> J. SILBER,<sup>17</sup> D. SPRAYBERRY,<sup>23</sup> G. TARLÉ,<sup>39</sup>  
B. A. WEAVER,<sup>23</sup> AND R. ZHOU<sup>17</sup>

- <sup>1</sup>David A. Dunlap Department of Astronomy & Astrophysics, University of Toronto, 50 St George Street, Toronto ON M5S 3H4, Canada  
<sup>2</sup>Dunlap Institute for Astronomy & Astrophysics, University of Toronto, 50 St George Street, Toronto, ON M5S 3H4, Canada  
<sup>3</sup>Departamento de Astrofísica, Universidad de La Laguna (ULL), E-38206, La Laguna, Tenerife, Spain  
<sup>4</sup>Instituto de Astrofísica de Canarias, C/ Vía Láctea, s/n, E-38205 La Laguna, Tenerife, Spain  
<sup>5</sup>Steward Observatory, University of Arizona, 933 N, Cherry Ave, Tucson, AZ 85721, USA  
<sup>6</sup>Observatório Nacional, Rio de Janeiro - RJ, 20921-400, Brasil  
<sup>7</sup>Institute for Astronomy, University of Edinburgh, Royal Observatory, Blackford Hill, Edinburgh EH9 3HJ, UK  
<sup>8</sup>Department of Astronomy & Astrophysics, University of Toronto, Toronto, ON M5S 3H4, Canada  
<sup>9</sup>Institute of Astronomy, University of Cambridge, Madingley Road, Cambridge CB3 0HA, UK  
<sup>10</sup>Department of Astronomy & Astrophysics, University of California, Santa Cruz, Santa Cruz, CA 95064, USA  
<sup>11</sup>NSF NOIRLab, 950 N. Cherry Avenue, Tucson, AZ 85719, USA  
<sup>12</sup>Department of Astronomy and Astrophysics, UCO/Lick Observatory, University of California, 1156 High Street, Santa Cruz, CA 95064, USA  
<sup>13</sup>Department of Astronomy and Astrophysics, University of California, Santa Cruz, 1156 High Street, Santa Cruz, CA 95065, USA  
<sup>14</sup>University of California Observatories, 1156 High Street, Sana Cruz, CA 95065, USA  
<sup>15</sup>Institute of Astronomy and Department of Physics, National Tsing Hua University, 101 Kuang-Fu Rd. Sec. 2, Hsinchu 30013, Taiwan  
<sup>16</sup>Institute for Computational Cosmology, Department of Physics, Durham University, South Road, Durham DH1 3LE, UK  
<sup>17</sup>Lawrence Berkeley National Laboratory, 1 Cyclotron Road, Berkeley, CA 94720, USA  
<sup>18</sup>Department of Physics, Boston University, 590 Commonwealth Avenue, Boston, MA 02215 USA  
<sup>19</sup>Dipartimento di Fisica “Aldo Pontremoli”, Università degli Studi di Milano, Via Celoria 16, I-20133 Milano, Italy  
<sup>20</sup>INAF-Osservatorio Astronomico di Brera, Via Brera 28, 20122 Milano, Italy  
<sup>21</sup>Department of Physics & Astronomy, University College London, Gower Street, London, WC1E 6BT, UK  
<sup>22</sup>Instituto de Física, Universidad Nacional Autónoma de México, Circuito de la Investigación Científica, Ciudad Universitaria, Cd. de México C. P. 04510, México  
<sup>23</sup>NSF NOIRLab, 950 N. Cherry Ave., Tucson, AZ 85719, USA  
<sup>24</sup>Departamento de Física, Universidad de los Andes, Cra. 1 No. 18A-10, Edificio Ip, CP 111711, Bogotá, Colombia  
<sup>25</sup>Observatorio Astronómico, Universidad de los Andes, Cra. 1 No. 18A-10, Edificio H, CP 111711 Bogotá, Colombia  
<sup>26</sup>Institut d’Estudis Espacials de Catalunya (IEEC), c/ Esteve Terradas 1, Edifici RDIT, Campus PMT-UPC, 08860 Castelldefels, Spain  
<sup>27</sup>Institute of Cosmology and Gravitation, University of Portsmouth, Dennis Sciama Building, Portsmouth, PO1 3FX, UK  
<sup>28</sup>Institute of Space Sciences, ICE-CSIC, Campus UAB, Carrer de Can Magrans s/n, 08913 Bellaterra, Barcelona, Spain  
<sup>29</sup>Fermi National Accelerator Laboratory, PO Box 500, Batavia, IL 60510, USA  
<sup>30</sup>Department of Physics, The University of Texas at Dallas, 800 W. Campbell Rd., Richardson, TX 75080, USA  
<sup>31</sup>Department of Physics, Southern Methodist University, 3215 Daniel Avenue, Dallas, TX 75275, USA  
<sup>32</sup>Sorbonne Université, CNRS/IN2P3, Laboratoire de Physique Nucléaire et de Hautes Energies (LPNHE), FR-75005 Paris, France  
<sup>33</sup>Institució Catalana de Recerca i Estudis Avançats, Passeig de Lluís Companys, 23, 08010 Barcelona, Spain  
<sup>34</sup>Institut de Física d’Altes Energies (IFAE), The Barcelona Institute of Science and Technology, Edifici Cn, Campus UAB, 08193, Bellaterra (Barcelona), Spain  
<sup>35</sup>Instituto de Astrofísica de Andalucía (CSIC), Glorieta de la Astronomía, s/n, E-18008 Granada, Spain

<sup>36</sup>*Departament de Física, EEBE, Universitat Politècnica de Catalunya, c/Eduard Maristany 10, 08930 Barcelona, Spain*

<sup>37</sup>*Department of Physics and Astronomy, Sejong University, 209 Neungdong-ro, Gwangjin-gu, Seoul 05006, Republic of Korea*

<sup>38</sup>*CIEMAT, Avenida Complutense 40, E-28040 Madrid, Spain*

<sup>39</sup>*University of Michigan, 500 S. State Street, Ann Arbor, MI 48109, USA*

## ABSTRACT

RR Lyrae stars (RRLs) are valuable probes of both Milky Way assembly and stellar-evolution physics. Using a sample 6,240 RRLs obtained in the first year of the Dark Energy Spectroscopic Instrument (DESI) survey, we investigate the metallicity of RRLs and its correlation with their pulsation properties. We find that (1) a clear correlation between period and  $[\text{Fe}/\text{H}]$  reinforces the view that the long-standing Oosterhoff dichotomy arises from the scarcity of intermediate-metallicity Galactic globular clusters hosting sizeable RRL samples; (2) high-amplitude short-period and small-amplitude short-period variables are comparatively metal-rich, with mean  $[\text{Fe}/\text{H}] = -1.39 \pm 0.27$  and  $-1.30 \pm 0.28$ , respectively; (3) in double-mode pulsators (RRd) the metallicity declines smoothly with increasing fundamental-mode period, and anomalous RRd stars occupy a remarkably narrow  $[\text{Fe}/\text{H}]$  range relative to classical RRd stars; (4) this spectroscopic sample let us, for the first time, place empirical constraints on the metallicity-dependent topology of the instability strip using phase-corrected effective temperatures and a large number of RRLs, where we observe an instability strip that moves towards cooler  $T_{\text{eff}}$  with declining  $[\text{Fe}/\text{H}]$  with a width consistent with stellar-evolution models; and (5) a subset of metal-rich RRLs exhibits orbits consistent with disk membership and halo kinematics. Our results confirm the tantalizing potential of DESI for Galactic and stellar astrophysics and highlight the importance of the even larger samples of RRLs and data-processing improvements forthcoming in future DESI data releases.

*Keywords:* Dwarf galaxies(416), Globular star clusters(656), Halo stars(699), Instability strip(798), Milky Way Galaxy(1054), Milky Way stellar halo(1060), RR Lyrae variable stars(1410), Spectroscopy(1558), Stellar kinematics(1608)

## 1. INTRODUCTION

RR Lyrae stars (hereafter RRLs; RRL for a single star) play a pivotal role in unraveling the formation history of our Galaxy, the Milky Way, and serve as key benchmarks for advancing our understanding of stellar evolution (Bono & Stellingwerf 1994; Catelan 2009). These low-mass variable stars are predominantly old and metal-poor (Population II) stars, commonly found in the Galactic halo (e.g., Zinn et al. 2014; Torrealba et al. 2015; Sesar et al. 2017; Medina et al. 2018; Stringer et al. 2021; Medina et al. 2024), globular clusters (e.g., Bailey & Pickering 1913; Castellani et al. 2003; Navarrete et al. 2015; Kundu et al. 2019; Cruz Reyes et al. 2024), and dwarf galaxies (e.g., Medina et al. 2017; Martínez-Vázquez et al. 2019; Torrealba et al. 2019; Vivas et al. 2020; Monelli & Fiorentino 2022), and are widely known as precise distance indicators (Catelan & Smith 2015; Beaton et al. 2018). They lie in the intersection between the horizontal branch and instability strip in the Hertzsprung-Russel (HR) diagram, and are characterized by their short periods of pulsation ( $< 1$  d).

RR Lyrae variables can be divided into three main subclasses. The most numerous among different RRL classes pulsate in the fundamental mode (ab-type RRLs;

RRab), with saw-tooth shaped light curves, periods ranging from 0.4 d to 1.0 d, and amplitudes that anti-correlate with period and reach up to  $\sim 1.2$  mag in the  $V$ -band. RR Lyrae variables that pulsate in the first-overtone mode, (c-type RRLs; RRc), display shorter periods than RRab stars (0.25-0.40 d) with smaller amplitudes ( $< 0.7$  mag in the  $V$ -band). The third subclass (d-type RRLs; RRd) is significantly less common than RRab and RRc. Stars in this class pulsate in both the fundamental and the first-overtone mode, the latter being the dominant one (Nemec 1985; Bono et al. 1996; Nemec et al. 2024). For most RRd stars, the first-overtone pulsation displays larger amplitude than the fundamental mode component, with first-overtone light curves that resemble those of single-mode RRc stars. The position of the RRL subtypes in the HR diagram is a good diagnostic tool for constraining the shape of the instability strip (see Catelan & Smith 2015, and references therein). Indeed, according to stellar evolution models, RRab stars are located closer to the cooler (red) edge of the instability strip in the HR diagram, as they occur directly after the ignition of helium in the stars' cores (see e.g., Bono & Stellingwerf 1994). Conversely,

RRc stars lie towards the hotter (blue) edge of the instability strip, and RRd stars lie in the intermediate region.

The chemical abundance patterns of RRLs, and iron abundance in particular, play an important role in their evolution and their use as stellar population tracers in the local universe. For instance, what makes RRLs excellent distance indicators is the tight correlation between their periods of pulsation, metallicities, and luminosity in the infrared, and their luminosity-metallicity relation in optical bands. These correlations have been extensively studied empirically (e.g., Muraveva et al. 2015; Sesar et al. 2017; Garofalo et al. 2022; Prudil et al. 2024; Narloch et al. 2024) and with the use of stellar evolution models (e.g., Bono et al. 2003; Catelan et al. 2004; Neeley et al. 2017; Marconi et al. 2022), and their calibration relies on the choice of a given metallicity scale. The iron abundance of RRLs also plays a role in the shape of their light curves, as measured by their Fourier decomposition, which is reflected in known correlations between the phase parameter  $\phi_{31}$  (defined using the first and third Fourier coefficients,  $\phi_1$  and  $\phi_3$ ), their periods, and  $[\text{Fe}/\text{H}]$  (see e.g., Jurcsik & Kovacs 1996; Smolec 2005; Nemeč et al. 2013; Dékány et al. 2021; Mullen et al. 2021, 2022). Moreover, the morphology of the horizontal branch, and therefore, the depth of its incursion into the instability strip (at a fixed age) is highly dependent on metallicity (see e.g., Savino et al. 2020), and even the topology of the instability strip is a function of metallicity (Marconi et al. 2015). Furthermore, the smooth gradient in metallicity as a function of period observed among field RRLs (Fabrizio et al. 2019, 2021) and the link between (high metallicity) short-period RRLs and massive Milky Way satellites (Fiorentino et al. 2015; Monelli & Fiorentino 2022) provide valuable insights into the origin of the halo. Additionally, the presence of RRLs with anomalously high  $[\text{Fe}/\text{H}]$  in the Milky Way might suggest the existence of alternative formation mechanisms for these stars (e.g., Bono et al. 1997a,b; Bobrick et al. 2024). A major limitation in performing statistically robust empirical studies in any of these research areas is the strong requirement for access to sizable samples of RRLs with uniformly determined metallicities.

The Dark Energy Spectroscopic Instrument (DESI; DESI Collaboration et al. 2016a,b, 2022) Milky Way survey provides a unique dataset to study the spectroscopic properties of RRLs, and, in particular, their chemical abundances. DESI is mounted at the Mayall 4-m telescope at Kitt Peak National Observatory and is composed of 5000 robotic fibers that feed ten thermally-controlled 3-channel spectrographs, covering a wavelength range of 3600 to 9800 Å with a resolution

of  $\sim 2000 - 5000$  ( $\sim 1.8$  Å). While DESI’s main scientific goal is to perform cosmological studies of the large-scale structure of the universe and its expansion (see e.g., Levi et al. 2013; DESI Collaboration et al. 2024, 2025a), DESI has also observed several millions of stars in the Galactic disk and the halo as part of the bright-time Milky Way survey (see e.g., Cooper et al. 2023; Koposov et al. 2024). Indeed, recent works that reveal the tremendous potential of DESI for Milky Way science include the use of blue horizontal-branch (BHB) stars (Byström et al. 2024) to characterize the bulk motion of the Milky Way disk caused by the influence of the Large Magellanic Cloud (LMC), the study of nearby substructures in the Galactic halo (Kim et al. 2025), the compilation of white dwarf catalogs and identification of new white dwarf classes (Manser et al. 2023, 2024), and the identification of metal-poor stars (Allende Prieto et al. 2023). More specifically, thousands of RRLs with homogeneously-derived spectroscopic properties ( $[\text{Fe}/\text{H}]$ ,  $T_{\text{eff}}$ ,  $\log g$ , and center-of-mass radial velocities) were observed in DESI’s first year of operation. A detailed analysis of the DESI Year 1 (Y1) RRL catalog, which contains thousands of RRab and RRc stars, and hundreds of RRd stars, is presented in a companion paper (Medina et al. 2025, hereafter M25)

In this paper, we use the  $[\text{Fe}/\text{H}]$  measurements in the DESI Y1 database (M25) to study the metallicity of RRLs and its correlation with their periods and amplitudes, and with the position and width of the RRL instability strip. Additionally, we inspect the database and identify a subsample of stars with relatively high iron abundances ( $[\text{Fe}/\text{H}] > -0.5$  dex). In Section 2, we introduce the reader to the DESI survey, with an emphasis on its Y1 RRL catalog. Section 3 describes the correlations between  $[\text{Fe}/\text{H}]$  and the periods and amplitudes of RRLs visible in the data, addressing the so-called Oosterhoff dichotomy, and the iron abundance and origin of short-period RRab and RRc. The metallicity dependence of the periods of pulsation of double-mode RRLs is described in Section 4. Section 5 details the observed dependency of the shape and width of the instability strip with metallicity from our RRL sample, and contrasts them with those predicted by stellar evolution models. In Section 6, we study the metal-rich end of the DESI RRL metallicity distribution, and discuss possible explanations for the stars in this regime. Lastly, we summarize our findings in Section 7.

## 2. DATA

### 2.1. The DESI RRL catalog

The DESI Milky Way Survey (DESI-MWS) targets RRLs from the *Gaia* Data Release 2 (DR2; Clementini

et al. 2019) and the Pan-STARRS1 (PS-1; Sesar et al. 2017) catalogs. These RRLs were observed as primary and secondary targets in the commissioning, science verification, and main component of DESI, primarily as part of its bright and dark programs. An overview of the DESI survey, its observing strategy, and data processing pipelines are provided by Guy et al. (2023), Schlafly et al. (2023), Miller et al. (2024) and Poppett et al. (2024). For a comprehensive description of DESI-MWS, including details of its data products, we refer the reader to Cooper et al. (2023) and Koposov et al. (2024). Further details of the RRL catalog, including a validation of the spectroscopic properties discussed in this paper, are presented by M25.

The RRL catalog used in this work was compiled by M25, taking advantage of DESI’s high observing efficiency, wide wavelength coverage, and the large footprint of the survey. This catalog is based on observations taken by the DESI survey during its first year of operation (Y1), which correspond to DESI’s first data release (DR1; DESI Collaboration et al. 2025b). The catalog was assembled by crossmatching the DESI database with the *Gaia* DR3 RRL catalog (Clementini et al. 2023) and is composed of 6,240 RRLs, representing one of the largest catalogs with homogeneously-derived spectroscopic properties available to date (other surveys targeting large numbers of RRLs include LAMOST, GALAH, and APOGEE; Deng et al. 2012; De Silva et al. 2015; Majewski et al. 2017). The catalog includes spectroscopic properties corrected by the pulsation component of each RRL (one of the biggest challenges in the study of the spectra of RRLs), including systemic (i.e., center-of-mass) velocities, effective temperatures ( $T_{\text{eff}}$ ), surface gravities ( $\log g$ ), and chemical abundances ( $[\text{Fe}/\text{H}]$  and  $[\alpha/\text{Fe}]$ ). For a detailed description of the methodology used to correct the line-of-sight velocities and  $T_{\text{eff}}$  of the sample for their expected variations throughout the RRL pulsation cycle, which can easily reach  $\sim 60 \text{ km s}^{-1}$  and 1,000 K for a given RRL (respectively), we refer the reader to M25. For DESI, velocities and atmospheric parameters are computed using DESI’s data processing pipelines, namely RVS (Koposov 2019a) (used for single epoch and coadded spectra) and SP (Allende Prieto et al. 2006) (for coadded spectra). Moreover, the DESI Y1 RRL catalog includes  $[\text{Fe}/\text{H}]$  derived using the recent calibration of so-called  $\Delta S$  method (Preston 1959) presented by Crestani et al. (2021a), which relates the equivalent widths of Balmer lines and the Ca K line with the  $[\text{Fe}/\text{H}]$  of RRLs. In this work, we rely mostly on the  $[\text{Fe}/\text{H}]$  from RVS, which are derived using the Python package RVSpecfit (Koposov et al. 2019) based on the fitting of interpolated synthetic spectra from PHOENIX

model atmospheres (Husser et al. 2013). A Bayesian inference methodology is then employed to estimate the systemic velocities and mean  $T_{\text{eff}}$  of the RRLs, from which the variation of these properties throughout the RRL pulsation cycle is modeled. This enables the estimation of these properties even from single-epoch measurements.

The best classification of the RRLs in the DESI Y1 sample and their overall variability properties (e.g., periods and amplitudes of pulsation), are taken directly from the *Gaia* DR3 catalog. Based on this classification, 4,524 (72%) RRLs in our sample are fundamental mode pulsators, 1,609 (26%) are first-overtone pulsators, and 107 (2%) are double mode pulsators.

The DESI Y1 catalog contains RRLs with heliocentric distances ( $d_{\text{H}}$ ) ranging between 2 and 115 kpc. In terms of Galactocentric distances  $R_{\text{GC}}$ , calculated adopting a spheroidal halo and a distance of 8.275 kpc from the Sun to the Galactic center (GRAVITY Collaboration et al. 2021), the sample covers a range of 3 to 120 kpc. Thus, this catalog reaches regions well beyond the inner halo and with a significant coverage of the outer halo. These RRLs span a wide range of iron abundances, from  $-3.70$  to  $-0.10$  dex.

A significant fraction of the RRLs in our catalog can be associated with known stellar systems and substructures. Indeed, M25 determined that 600 are likely part of the Sagittarius (Sgr) stream, 2,134 have velocities and  $[\text{Fe}/\text{H}]$  consistent with the Gaia-Sausage-Enceladus (GSE) merger progenitor, and 86 are high probability members of dwarf spheroidal galaxies or globular clusters (including Draco, Ursa Major II, Bootes III, Palomar 5, NGC 5904, NGC 5466, NGC 5024, NGC 5053, NGC 6341, NGC 2419, NGC 4147, and NGC 5634). Of the latter, the most notable is the Draco dwarf spheroidal galaxy, containing 59 DESI Y1 RRLs.

## 2.2. Orbital parameters

To determine the dynamical properties of the RRLs in our sample (which are relevant for Sections 3 and 6), we model their orbits using the Python module GALPY (Bovy 2015)<sup>1</sup> integrating the orbits for 5 Gyr backwards in time. To model the Galactic potential, we adopt GALPY’s built-in *MWPotential2014*, which consists of a spherical nucleus and bulge (Hernquist potential; Hernquist 1990), a Miyamoto-Nagai disk model (Miyamoto & Nagai 1975), and a spherical Navarro-Frenk-White dark matter halo (Navarro et al. 1997). Additionally, we considered the impact of the LMC on

<sup>1</sup> <http://github.com/jobovy/galpy>

the Milky Way potential, given the growing evidence that indicate its significant effects for modeling orbits (see e.g., Erkal et al. 2018; Cunningham et al. 2020; Vasiliev et al. 2021; Medina et al. 2023). For the current position of the LMC, we used  $\alpha = 78.77$  deg and  $\delta = -69.01$  deg as central equatorial coordinates, and a distance of  $d_{\text{LMC}} = 49.6$  kpc (Pietrzyński et al. 2019). For its current motion, we adopted a systemic line-of-sight velocity of  $262.2 \text{ km s}^{-1}$  (van der Marel et al. 2002) and proper motions of  $\mu_\alpha = 1.850 \text{ mas yr}^{-1}$  and  $\mu_\delta = 0.234 \text{ mas yr}^{-1}$  (Gaia Collaboration et al. 2018). We assumed an LMC mass of  $1.88 \times 10^{11} M_\odot$  (Shipp et al. 2021) and a scale length  $a_{\text{LMC}} = 20.22$  kpc, which recovers the circular velocity at 8.7 kpc from the LMC center observed by van der Marel & Kallivayalil (2014). To account for the fact that the LMC is not bound to the Milky Way in *MWPotential2014*, we multiply the Milky Way halo mass by a factor of 1.5 (which makes the LMC bound to the Galaxy<sup>2</sup>). Lastly, we consider the effect of Chandrasekhar dynamical friction in the LMC’s orbit integration, and ignore the gravitational perturbations caused by other massive Milky Way satellites.

The orbital parameters of the RRLs in our sample and their uncertainties are obtained using *Gaia* DR3 proper motions and DESI-derived systemic velocities and heliocentric distances (M25). We perform 500 GALPY realizations per star, varying the input systemic velocities, heliocentric distances, and proper motions of the orbits assuming that they follow Gaussian distributions with standard deviations equal to their observed uncertainties. Proper motion uncertainties and their covariances are obtained directly from *Gaia* DR3, whereas systemic velocity and heliocentric distance uncertainties are derived from DESI’s radial velocity curve modeling and error propagation, respectively (see M25). The orbital parameters and their uncertainties correspond to the median of the resulting distributions and their 16 and 84 percentiles, respectively.

### 3. THE BAILEY DIAGRAM

The position of RRLs in the period-amplitude space, the so-called Bailey diagram, offers a valuable perspective to study the physics of their pulsation and the formation of the halo (see e.g., Fiorentino et al. 2015, 2017; Belokurov et al. 2018; Fabrizio et al. 2019; Bono et al. 2020). In this diagram, first-overtone pulsators are clumped in its short-period, low-amplitude region, whereas RRab variables are characterized by larger amplitudes and longer periods than RRcs (overall), with lu-

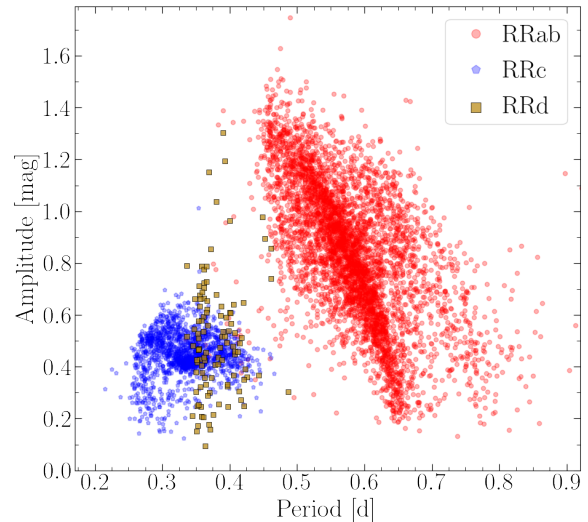


**Figure 1.** Bailey diagram of the DESI Y1 RRL sample (adapted from M25). The light curve amplitudes in the  $V$ -band ( $A_V$ ) shown are computed using the peak-to-peak  $G$ -band magnitudes listed in the *Gaia* catalog and the transformation equation from Clementini et al. (2019). The classification of RRLs between RRab, RRc, and RRd is taken directly from the *Gaia* DR3 catalog (Clementini et al. 2023).

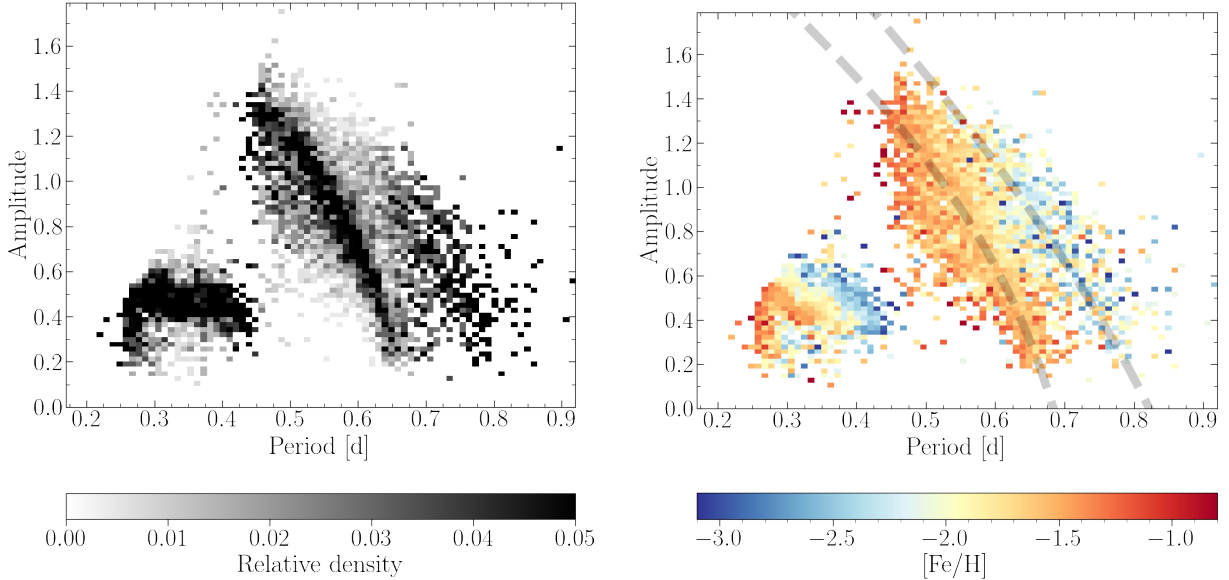
minosity amplitudes decreasing with increasing periods. The distribution of RRLs in the Bailey diagram depends on their physical properties (evolutionary phase, mass, luminosity, effective temperature) and chemical composition, as well as the existence of secondary modulations and non-linear pulsation phenomena (e.g., shocks; Bono et al. 2020).

Figure 1 depicts the Bailey diagram for the DESI Y1 sample for RRab, RRc, and RRd variables, using the periods provided in the *Gaia* DR3 catalog and  $V$ -band pulsation amplitudes ( $A_V$ ). For the latter, we adopt the prescription of Clementini et al. (2019) to transform the peak-to-peak amplitudes reported by *Gaia*,  $A_G$  (PEAK\_TO\_PEAK\_G in *Gaia*) to  $V$ -band amplitudes, i.e.,  $A_V = (1.081 \pm 0.003) A_G + (0.013 \pm 0.003)$ . Figure 1 shows clearly the separation between the RRL subtypes, from their classification in the *Gaia* catalog. In the rest of this section, we analyze two science questions related to the position of the DESI Y1 RRL sample in the Bailey diagram.

#### 3.1. On the Oosterhoff dichotomy and $[Fe/H]$ dependencies in the Bailey diagram

One of the most intriguing and long-standing problems related to the position of RRLs in the Bailey diagram is the so-called Oosterhoff dichotomy (see e.g., Caputo et al. 1989; Bono et al. 1994, 1995b; Lee & Car-

<sup>2</sup> <https://docs.galpy.org/en/stable/orbit.html>



**Figure 2.** Same as Figure 1 but as a column normalized histogram (*left*, i.e. the sum of the density in each column is one) and color-coded by the average  $[\text{Fe}/\text{H}]$  in each pixel (*right*). In the right plot, dashed lines are used to represent the position of the fiducial curves for OoI and OoII defined by Fabrizio et al. (2019). The position of the OoI and OoII lines is consistent with the location of the bulk of the more metal rich ( $[\text{Fe}/\text{H}] > -2.0$  dex) and more metal-poor ( $[\text{Fe}/\text{H}] < -2.0$  dex) RRab population in the Bailey diagram, respectively.

ney 1999; Cassisi et al. 2004). The Oosterhoff dichotomy was first reported by Oosterhoff (1939), who recognized that RRLs in globular clusters could be mainly separated into two groups: one with RRab variables with periods  $\leq 0.55$  d (Oosterhoff I, or OoI), and the other with RRab periods closer to 0.65 (Oosterhoff II, or OoII). It was later recognized that this dichotomy is also reflected in the fraction of RRc with respect to the total number of RRLs in the clusters, with a larger fraction corresponding to OoII (see e.g., Braga et al. 2016). Furthermore, OoI clusters have been found to be more metal-rich than those in the OoII group ( $[\text{Fe}/\text{H}] \sim -1.3$  vs.  $\sim -2.0$  dex, respectively; Catelan & Smith 2015 and references therein). On the other hand, RRab stars in dwarf galaxies tend to populate the period gap between the two Oosterhoff groups (the *Oosterhoff gap*), in the so-called Oosterhoff-intermediate (Oo-int) region, and field stars are predominantly OoI (Catelan & Smith 2015). Thus, the fact that RRab in dwarf galaxies and in the field do not follow the dichotomy, together with findings of dissimilar chemical enrichment histories between globular clusters and the Milky Way halo (see e.g., Carretta et al. 2009), gives us insight into the role of globular clusters in the formation of the Galactic halo.

The homogeneous dataset provided by DESI offers a unique opportunity to inspect metallicity variations in the Bailey diagram and to study their association with

the Oosterhoff dichotomy. For this analysis, we employ the iron abundances obtained with DESI’s RVS processing pipeline. The left panel of Figure 2 depicts the Bailey diagram of the DESI Y1 RRL sample as a column-normalized histogram, showing two distinctive groups of RRab stars associated with the two Oosterhoff groups. The right panel of Figure 2 shows the correlation of the position of the RRL in the period- $A_V$  with their iron abundance. In the right panel, the fiducial OoI and OoII lines defined by Fabrizio et al. (2019) using a similarly large dataset (for RRab stars) are included, showing an overall good agreement with our data. We note in passing that our sample is composed predominantly of field stars, of which a significant fraction exhibits chemodynamics consistent with the GSE accretion event. These stars are mainly associated with the OoI group. Among the RRab in intact satellites, those in Draco are the most numerous (46 stars), and exhibit a mean period of  $0.60 \pm 0.07$  d. The fundamental-mode RRLs (RRab) in GCs are less numerous (16 stars), but seem to be consistent with the dichotomy with a preferential location towards the locus of the OoII group (as shown later in Figure 5), with a mean period of their RRab of  $0.64 \pm 0.08$  d. Similar to the RRab in Draco, those in the Sgr stream display  $0.59 \pm 0.06$  d periods broadly consistent with the OoI group.

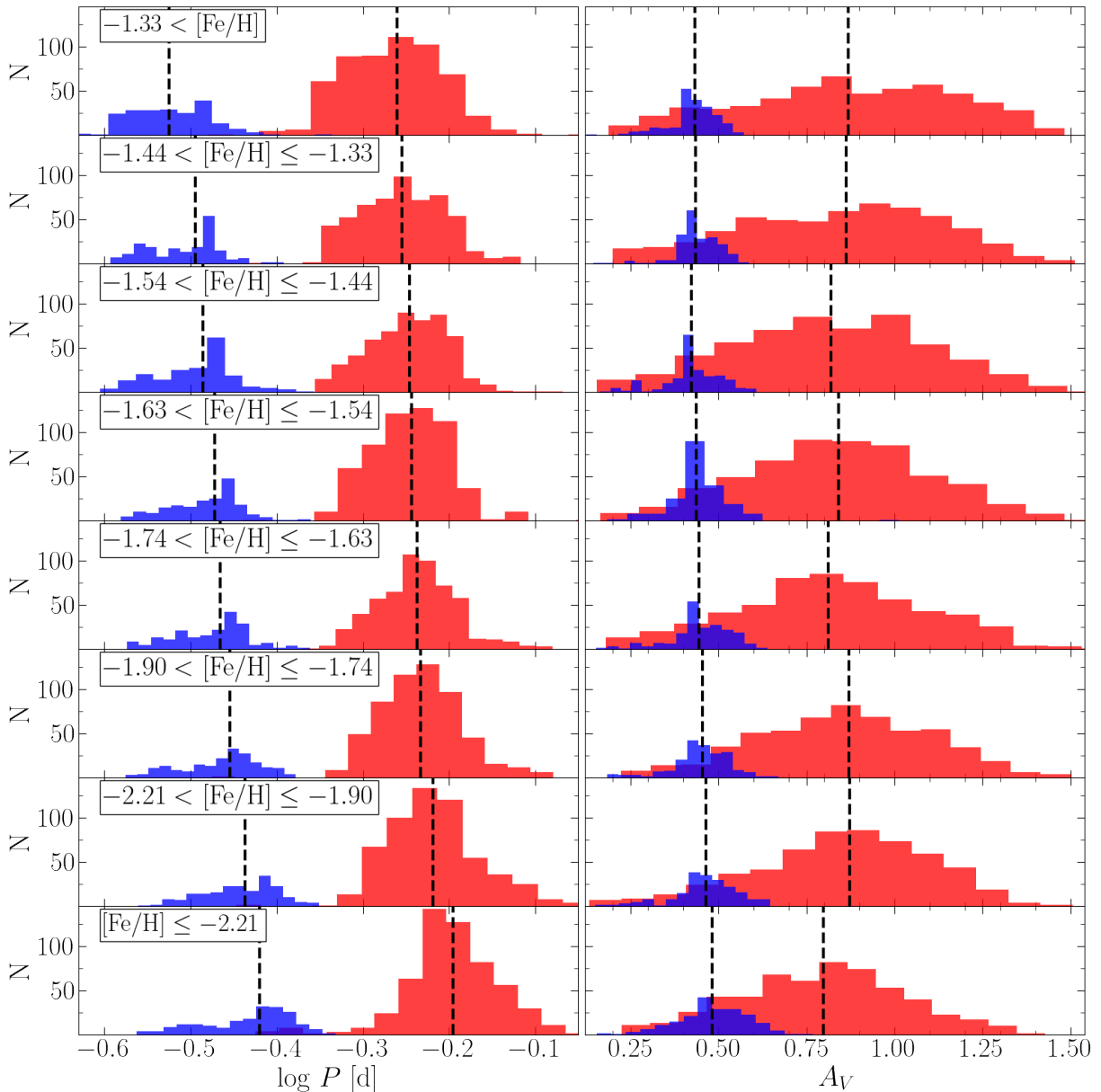


**Figure 3.** Distribution of  $\log P$  (left panels) and visual amplitude  $A_V$  (right panels) of the DESI Y1 RRL sample as a function of iron abundance. To illustrate existing correlations, the data is split into eight metallicity bins containing the same number of stars. In each panel, a blue histogram is used to represent RRC stars, whereas the  $\log P$  and  $A_V$  distribution of RRab is shown in red (towards longer periods and higher amplitudes). Dashed vertical lines display the median of each distribution. The left-hand panels show a systematic shift in  $\log P$  from the more metal-rich to the more metal-poor regime towards long periods, both for RRab and RRC. This trend is more subtle for the visual amplitudes of RRC and not observed for RRab.

In Figure 2, we observe a smooth decline in metallicity (from the metal-rich to the metal-poor end of the RRL distribution) as the period of pulsation increases, at any given  $A_V$  and for both RRab and RRC. For a direct comparison with the period and  $A_V$   $[\text{Fe}/\text{H}]$  correlations recently reported by Fabrizio et al. (2021), we first follow their methodology and split our RRab and RRC samples in metallicity bins, each containing the same number of

stars. Here, however, we use eight bins per sub-class to ensure that we obtain a number of stars per bin similar to those of Fabrizio et al. (2021) (566 RRab and 202 RRC per metallicity bin).

Figure 3 displays the overall trends that the distribution of periods (left panels) and visual amplitudes (right panels), for each sub-class, follow as a function of  $[\text{Fe}/\text{H}]$ . The figure shows a steady decrease in period when mov-

ing from the metal-poor to the metal-rich regime, for both RRab and RRC stars. In fact, the median of the RRab and RRC  $\log P$  distributions (shown as vertical dashed lines in Figure 3) vary from  $\log P = -0.20$  d to  $\log P = -0.26$  d and from  $\log P = -0.42$  to  $\log P = -0.53$ , respectively, when the  $[\text{Fe}/\text{H}]$  varies from the most metal-poor to the metal-rich bins. These trends are more subtle in the  $A_V$  panels (right-hand plots) for RRC stars and no clear trend is visible for RRab stars.

In order to better quantify the  $[\text{Fe}/\text{H}]$  dependence of the periods and amplitudes, we repeat the experiment increasing the number of metallicity bins and using an equal number of stars per bin. We split the sample in 25  $[\text{Fe}/\text{H}]$  bins for RRab and RRC stars, each containing 181 and 65 stars, respectively. Then, we compute the median of the  $\log P$  and  $A_V$  of the stars in each bin, as well as their 16th and 84th percentiles. Figure 4 depicts the  $\log P$  and  $A_V$  of the entire sample as a function of  $[\text{Fe}/\text{H}]$ , as well as the median and percentiles in each bin, as described above. The figure shows that both visual amplitudes and periods of RRab and RRC stars vary smoothly over the studied metallicity range. We use these data to fit linear relations between the parameters with the Python package `scipy`, in the  $[\text{Fe}/\text{H}]$  range  $[-2.60, -1.19]$  dex for RRab stars, and  $[-2.79, -1.19]$  dex for RRC stars. It is noteworthy that such linear correlations are predicted by the pulsation relation when the evolutionary and pulsation properties of RRLs are taken into account (van Albada & Baker 1973; Caputo et al. 1998). The best fits for the correlations of each subtype are shown in Figure 4 with solid lines, and correspond to:

$$\begin{aligned} A_V &= 0.856 (\pm 0.041) + 0.007 (\pm 0.024) [\text{Fe}/\text{H}], \\ \log P &= -0.326 (\pm 0.005) - 0.052 (\pm 0.003) [\text{Fe}/\text{H}] \end{aligned} \quad (1)$$

for RRab stars and

$$\begin{aligned} A_V &= 0.377 (\pm 0.012) - 0.052 (\pm 0.003) [\text{Fe}/\text{H}], \\ \log P &= -0.594 (\pm 0.010) - 0.067 (\pm 0.005) [\text{Fe}/\text{H}] \end{aligned} \quad (2)$$

for RRC stars. These empirical relations indicate that a change of 1 dex in  $[\text{Fe}/\text{H}]$  results in a decrease of  $\sim 0.01$  and  $\sim 0.05$  mag in amplitude (on average) for RRab and RRC stars, and  $\sim 0.05$  and  $\sim 0.07$  dex in logarithmic period, respectively. We observe that the coefficients used for the metallicity dependence of the periods are roughly consistent between RRab and RRC stars (both being negative and statistically different than zero). A quick inspection of the figure shows, however, that although the visual amplitude and the metallicity of RRab

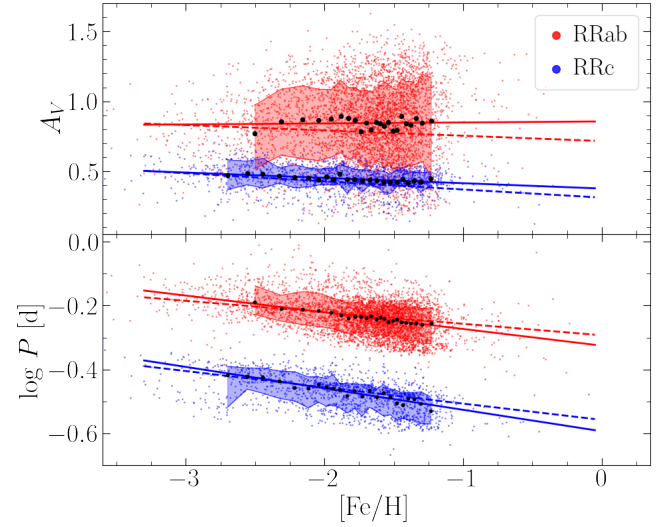


**Figure 4.** Iron-abundance dependence of the logarithm of the period and visual amplitude for RRab (red) and RRC (blue). The data is split into  $[\text{Fe}/\text{H}]$  bins with equal number of stars, in the range  $[-2.60, -1.19]$  dex for RRab stars, and  $[-2.79, -1.19]$  dex for RRC stars. In each panel, black filled circles are used to represent the median of the  $\log P$  or  $A_V$  distribution in each bin. Solid lines depict the best fit linear correlations for the medians computed per bin. Shaded regions show the 16th and 84th percentiles of each  $[\text{Fe}/\text{H}]$  bin. Dashed lines represent the  $A_V$ - $[\text{Fe}/\text{H}]$  and  $\log P$ - $[\text{Fe}/\text{H}]$  correlations reported by Fabrizio et al. (2021) using high-resolution and low-resolution ( $\Delta S$  method) spectra.

stars can be written as a rough correlation, the slope of the correlation is not significantly different from zero. In that regard, we note that RRab stars display a broad distribution of  $A_V$  values in each bin (as also seen in Figures 1 and 2) and large confidence intervals computed from the 16th and 84th percentiles for these stars (of the order of  $\sim 0.28$  mag), in comparison to those in the  $A_V$ - $[\text{Fe}/\text{H}]$  space of the RRC stars ( $\sim 0.16$  mag). This is also the case if we consider the peak-to-peak  $G$  amplitudes, taken directly from the *Gaia* catalog, instead of  $A_V$ . We consider the different behavior for the two types of RRLs significant regardless of the inherently different  $A_V$  for RRab and RRC stars. A tentative explanation for this difference is the impact of non-linear phenomena being stronger on fundamental-mode pulsators than on first-overtones (see e.g., Sneden et al. 2017; Gillet et al. 2019).

Our derived  $A_V$  and  $\log P$  anticorrelations with  $[\text{Fe}/\text{H}]$  can be compared with those found by Fabrizio et al. (2021) from a similarly large dataset. For RRab stars, we find almost no dependency of  $A_V$  on  $[\text{Fe}/\text{H}]$  (vs. a slope of  $-0.038$  mag dex $^{-1}$  in their work) and a stronger dependency in the case of  $\log P$  (by a factor of 1.4). In-

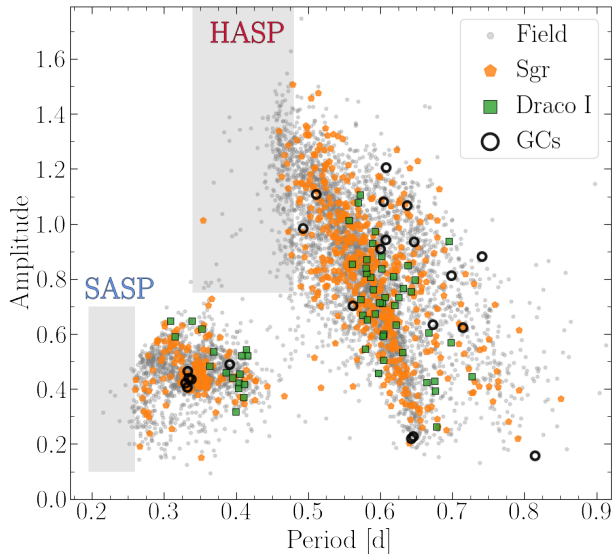


**Figure 5.** Bailey diagram of the DESI Y1 RRL sample separated by system. This distinction is made to better illustrate the distribution of RRLs in the halo, the Sagittarius stream (Sgr), Draco, and the combined sample of globular cluster RRLs. We note that the HASP region is dominated by field stars (with a few stars from Sgr), and the SASP region contains only field stars. This is in agreement with the general expectation for the origin of halo stars (see the text for more details).

Interestingly, for RRc variables the  $[\text{Fe}/\text{H}]$ -dependent factor on visual amplitude is just mildly smaller (by a factor of 1.1), but we find a similar difference in the logarithmic period as with the RRab (i.e., by a factor of 1.3). A potential explanation for the observed differences is that, although both of our works transform *Gaia*  $G$ -band amplitudes to the  $V$  band for deriving the correlations, we differ in the method used to estimate the  $G$  amplitudes, in the first place. More specifically, we use PEAK\_TO\_PEAK *Gaia* amplitudes whereas Fabrizio et al. (2021) adopt a combination of *Gaia* DR2-based analytical fit amplitudes and literature  $A_V$ . Moreover, we follow different methodologies to derive  $[\text{Fe}/\text{H}]$ . When using DESI’s  $\Delta S$ -based iron abundances, we find a much better agreement with their reported results for the zero-points and the slopes of these correlations (within  $1\sigma$ ), with the exception of the zero-point of our RRab  $A_V$ - $[\text{Fe}/\text{H}]$  relation (which differs from theirs by  $3\sigma$ ). This confirms the importance of the method for determining the  $[\text{Fe}/\text{H}]$  and  $G$ -band amplitude of the sample in the derived (empirical)  $A_V$ - $[\text{Fe}/\text{H}]$  relation for RRab stars.

Several recent studies have confirmed the complex nature of the Oosterhoff dichotomy, as a result of stellar and galactic evolution processes. Zhang et al. (2023),

for instance, indicated that the properties that define the Oosterhoff dichotomy vary with the position in the Galaxy and from galaxy to galaxy. Other studies have directly attributed the emergence of the Oosterhoff dichotomy to the accretion history of the Galaxy and/or RRL evolutionary effects (e.g., Luongo et al. 2024; Li et al. 2024), while others have linked the depopulation of the Oosterhoff gap to the mass of the accreted dwarf galaxies hosting globular clusters (Prudil & Ferro 2024). Fabrizio et al. (2019) and Fabrizio et al. (2021) provided an interpretation for the observed dichotomy, based on their reported anti-correlation between the position of RRLs in the Bailey diagram and their metallicities (for both RRab and RRc), observed as a steady decrease in their pulsation periods and in their visual amplitudes with increasing metallicity. These authors proposed the lack of metal-intermediate Galactic globular clusters hosting sizeable samples of RRL stars as a potential explanation for the dichotomy. Our reported anti-correlations (resulting from the extent of the instability strip exploration as a function of  $[\text{Fe}/\text{H}]$  and the period-density relation of RRLs) and the smooth transition from the long period (low metallicity) to the short period regime (high metallicity), together with the lack of intermediate metallicity Galactic globular clusters, provides a sensible explanation for the dichotomy, in line with the interpretation suggested by these authors.

### 3.2. HASPs and SASPs in DESI and the origin of the halo

As already discussed, the position of RRL variables in the Bailey diagram and their metallicities are important for their role as tracers of the halo formation and their connection with its building blocks. Indeed, several authors have shown that most Milky Way dwarf galaxy satellites lack high-amplitude short-period (HASP) RRab variables, that is, those with periods  $\leq 0.48$  d and visual amplitudes  $\geq 0.75$  mag, whereas they are typically observed in globular clusters (with  $[\text{Fe}/\text{H}] \geq -1.4$  dex) and in the halo field (Fiorentino et al. 2015, 2017; Monelli & Fiorentino 2022). This can be interpreted as a consequence of the correlation between these quantities and  $[\text{Fe}/\text{H}]$ , as the period distribution of RRab in relatively metal-rich globular clusters is shifted toward short periods (see e.g., Drake et al. 2013; Fiorentino et al. 2015). HASPs are also observed in the most massive Milky Way satellites (e.g., Sgr and the Magellanic Clouds), which suggests that the stars currently observed in most dwarf galaxies differ from the building blocks of the halo and that these building blocks were likely systems more massive than  $10^9 M_\odot$ .

In other words, the presence of HASPs in a system (determined solely by their position in the Bailey diagram) seems to be an indication of a fast early chemical enrichment, which allows the formation of old stars with  $[\text{Fe}/\text{H}] \geq -1.4$  dex. For an updated census of HASPs in dwarf galaxies and globular clusters, we refer the reader to Figure 7 in [Monelli & Fiorentino \(2022\)](#).

In a similar vein, small-amplitude short-period (SASP) RRc variables (those with periods  $< 0.26$  d) are not present in dwarf galaxies ([Fiorentino et al. 2022](#)), which also arises from the dependency between their periods and metal content. We note in passing that the existence of metal-rich RRLs is predicted from theoretical models, based on their pulsational and evolutionary properties (see [Bono et al. 1997a,b](#)). In fact, similar to HASPs, the period distribution of SASPs is only shifted toward short periods for RRc stars in massive satellites and in the halo (which corresponds to  $[\text{Fe}/\text{H}] \sim -1.4$  dex; [Crestani et al. 2021b](#)), another indication of the minor contribution of systems less massive than  $10^9 M_\odot$  to the formation of the halo.

Figure 5 shows the DESI Y1 Bailey diagram highlighting the HASP and SASP regions, making the distinction between RRLs in the halo field, the Sgr stream, Draco, and the combined sample of globular cluster RRLs. Here, following the convention from the literature, we define the HASP region as that with periods  $< 0.48$  d and  $A_V > 0.75$  mag, and the SASP region as that with periods  $< 0.26$  d and  $A_V > 0.1$  mag. It is clear from the figure that the HASP region is dominated by field stars. In fact, of the 270 RRab stars in this region, 97% are field stars, and only nine of them (3%) are from the Sgr stream. Similarly, 22 out of the 23 RRc stars in the SASP region are field stars (96%), and only one of them is from Sgr. For comparison, 88% of the non-HASP RRab stars are field RRLs, whereas for non-SASP RRc stars this fraction is 91%. Interestingly,  $\sim 60\%$  of the RRab in the HASP region display GSE membership probability  $p_{\text{GSE}} > 0.7$  (as reported by M25). For SASP RRc stars,  $\sim 40\%$  exhibit  $p_{\text{GSE}} > 0.7$ . There are no HASPs or SASPs in Draco and in globular clusters, following the expected trend.

To quantify the iron content distribution of short period RRLs, Figure 6 depicts  $[\text{Fe}/\text{H}]$  for our sample of HASPs and SASPs. As shown in the figure, the bulk of the metallicity distribution of both groups lies at  $-2.0 \leq [\text{Fe}/\text{H}] \leq -1.0$  dex, with a few outliers in both ends of the distribution. The median metallicity corresponds to  $-1.39$  dex and  $-1.30$  dex for HASPs and SASPs, with standard deviations of 0.27 dex and 0.28 dex, respectively. Thus, our results are consistent

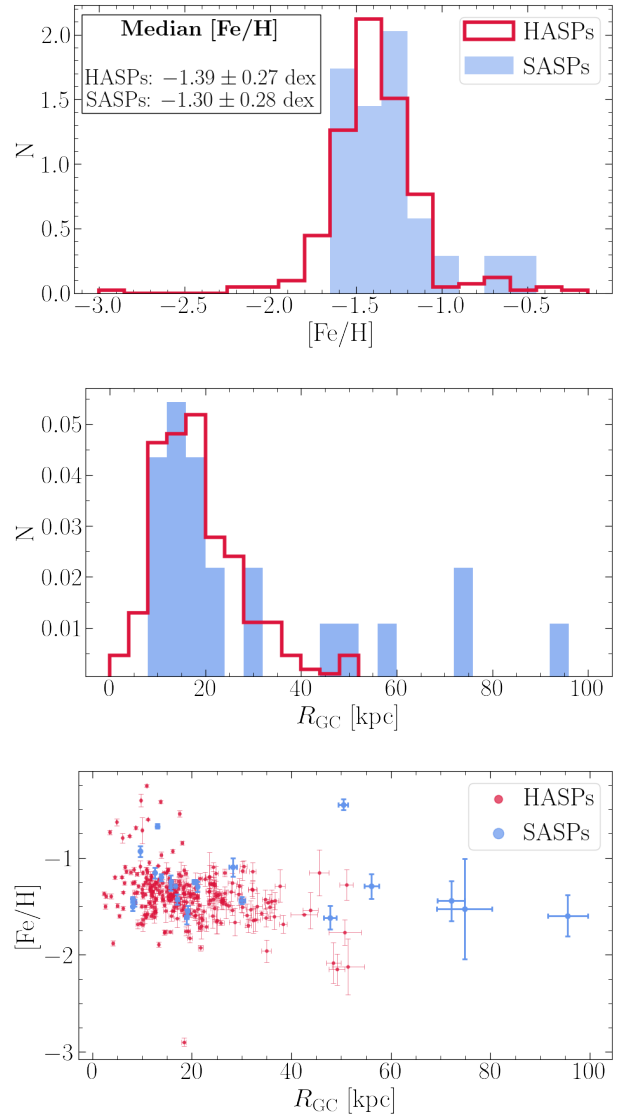


**Figure 6.** Normalized  $[\text{Fe}/\text{H}]$  (top) and Galactocentric distance (center) histograms of HASPs (red) and SASPs (blue) in the DESI Y1 RRL sample. The bottom panel displays the metallicity as a function of  $R_{\text{GC}}$  for both RRL subsamples.

with previous theoretical and empirical predictions for short-period RRLs.

Figure 6 also displays the distance distribution of the HASP and SASP samples. A marked decline in the distance distribution of these stars beyond  $\sim 30$  kpc is clear from the figure. This decline is specially clear for HASPs, which are more abundant than SASPs in our sample. However, we find a non-negligible fraction of these samples beyond this limit (31 HASPs and 7 SASPs). The outer halo of the Milky Way is predominantly composed of stars originating from the accretion of satellites (see e.g., [Naidu et al. 2020](#); [Medina et al.](#)

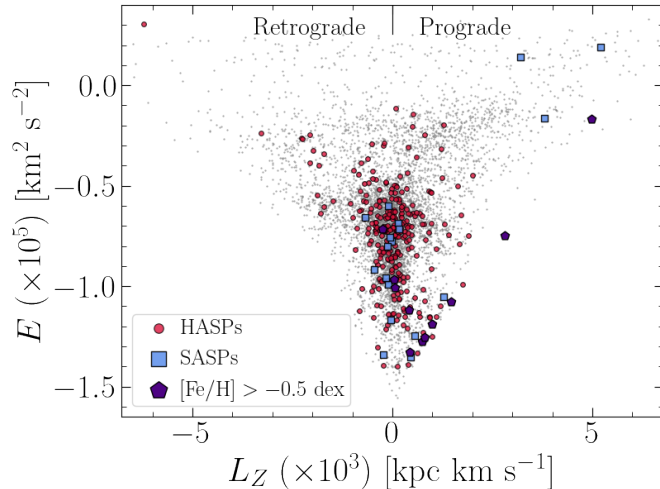


**Figure 7.** Vertical angular momentum  $L_Z$  and energy  $E$  of the stars in the DESI Y1 RRL sample, computed from the integration of their orbits using GALPY (Bovy 2015). Red, blue, and purple markers represent HASPs, SASPs, and RRLs with  $[\text{Fe}/\text{H}] > -0.5$  dex, respectively, whereas stars that do not fall in these categories are shown with grey dots.

2024). Since stars are not expected to form in-situ at these distances, and the aforementioned properties are suggestive of the nature of their origins, this sample displays strong evidence of having been accreted from massive satellites.

A group of HASPs and SASPs with  $[\text{Fe}/\text{H}] > -1$  dex is observed at  $R_{\text{GC}} < 20$  kpc. These stars are characterized by prograde motions and disk-like kinematics (based on their energies and angular momenta, as described later in this section). The figure also shows that our SASP sample reaches  $R_{\text{GC}} \sim 100$  kpc, whereas the HASP stars are only found out to  $R_{\text{GC}} \sim 50$  kpc. A possible explanation for the presence of SASPs beyond 50 kpc (and for the unexpectedly high  $[\text{Fe}/\text{H}]$  of a SASP at  $\sim 50$  kpc) is the contamination in the *Gaia* DR3 RRL catalog at large distances (e.g., by eclipsing binary stars). This suggestion is supported by the low score of the best class (RRc) reported by *Gaia* for these stars ( $\text{BEST\_CLASS\_SCORE} < 0.1$  for all of them). Additionally, the figure shows an outlier in the HASP metallicity distribution at  $R_{\text{GC}} \sim 20$  kpc, for which  $[\text{Fe}/\text{H}] \sim -2.9$  dex ( $\sim -3.3$  dex if measured by DESI’s SP pipeline, and  $\sim -1.5$  dex from the  $\Delta S$  method) with high signal-to-noise ratio  $S/N$  ( $\sim 65$ ) and relatively high  $\text{BEST\_CLASS\_SCORE}$  (0.82). This star, however, is flagged as an unsuccessful model fit by DESI’s SP pipeline likely due to data reduction. Lastly, we note that SASP stars and the bulk of the HASP sample follow the expected metallicity gradient of the DESI

RRLs in GSE (with a slope of  $0.005 \text{ dex kpc}^{-1}$ ; Figure 15 in M25), with larger scatter around this trend for HASPs at large distances ( $R_{\text{GC}} \geq 35$  kpc) likely due to number statistics. This supports their potential association with this merger event. We advocate for detailed high-resolution spectroscopic follow-up studies of the most distant HASPs and SASPs to confirm or reject their association with a massive progenitor via the expected high  $[\text{Fe}/\text{H}]$  observed for these stars as well as other chemical-abundance-based signatures, such as  $[\alpha/\text{Fe}]$  (e.g., by inspecting sequences extending from the metal-poor  $\alpha$ -enhanced regime to solar metallicities depleted in  $\alpha$  elements).

Figure 7 depicts the energy ( $E$ ) and vertical angular momentum ( $L_Z$ ) of our sample, highlighting the position of HASPs and SASPs in this space. The relative position of stars in this diagram serves as an indication of their dynamical origin, as stars with a common progenitor share similar integrals-of-motion due to the long timescales required for phase-space mixing in the halo. From their  $E$ - $L_Z$  distribution, it is clear that a significant fraction of these stars lie close to  $L_Z \sim 0 \text{ kpc km s}^{-1}$ , a region dominated by stars with radial orbits associated with the GSE merger event (as shown by M25). Together with the fraction of HASP and SASP stars with high  $p_{\text{GSE}}$  and the observed  $[\text{Fe}/\text{H}]$  as a function of  $R_{\text{GC}}$  (Figure 6), this supports the association of these stars with GSE. For the non-GSE HASPs, we observe a relatively homogeneous  $E$  and  $L_Z$  distribution, with  $E < 0 \text{ km}^2 \text{ s}^{-2}$  and displaying both prograde ( $L_Z > 0 \text{ kpc km s}^{-1}$ ) and retrograde ( $L_Z < 0 \text{ kpc km s}^{-1}$ ) orbits. Interestingly, this is not the case for our SASP sample, which show orbits that are preferentially prograde and relatively low energy ( $E < -0.5 \times 10^5 \text{ km}^2 \text{ s}^{-2}$ ; see Figure 7), with the exception of three stars, all of which lie at  $R_{\text{GC}} > 30$  kpc (two of them with  $\text{BEST\_CLASS\_SCORE} < 0.1$ ).

#### 4. DOUBLE-MODE PULSATORS AND $[\text{Fe}/\text{H}]$

The ratio of the first-overtone period to the fundamental mode period of RRd stars provides reddening independent insights on the physical properties of these stars. Indeed, the position of RRd stars in the first-overtone to fundamental period ratio ( $P_{1\text{O}}/P_{\text{F}}$ ) versus fundamental mode period ( $P_{\text{F}}$ ) space, the so-called Petersen diagram (Petersen 1973), has been extensively studied both empirically (see e.g., Soszyński et al. 2019; Chen et al. 2023; Braga et al. 2022) and theoretically (with the use of pulsation models; see e.g., Cox et al. 1980; Bono et al. 1996; Popielski et al. 2000). In the Petersen diagram, RRd stars follow a well-defined sequence, as a consequence of the impact of luminosity,

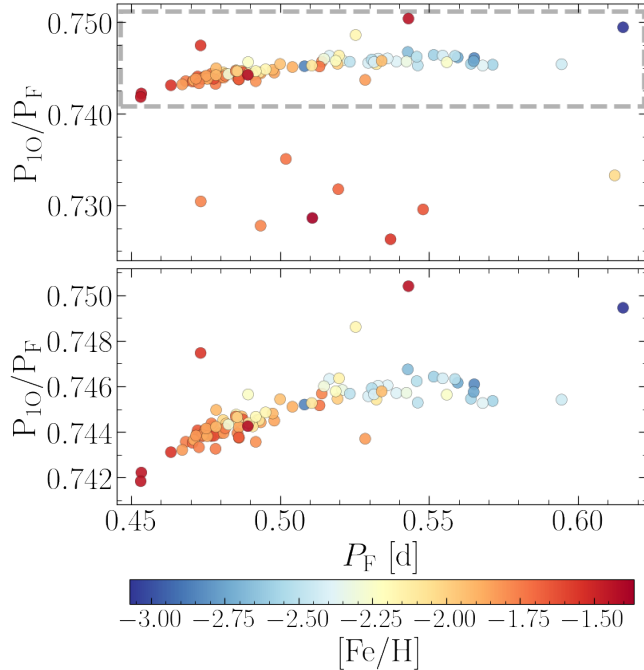


**Figure 8.** Period ratio (first-overtone period to fundamental-mode period) versus fundamental period for the (field) RRd stars observed in DESI Y1, color-coded by  $[\text{Fe}/\text{H}]$ . The *top* panel depicts a zoomed out version of the diagram, showing the presence of RRd stars with non-canonical period ratios. The *bottom* panel highlights the region where the bulk of the distribution lies (shown with a dashed rectangle in the top panel), with period ratios between  $\sim 0.742$  and  $\sim 0.750$  d.

stellar mass,  $T_{\text{eff}}$ , and chemical composition on these stars’ periods (stemming from the van Albada and Baker relations; van Albada & Baker 1971). Furthermore, “anomalous” RRd stars have been classified based on their position in the Petersen diagram, where they lie above or below the locus of the period ratio- $P_{\text{F}}$  distribution of “classical” RRd stars. These stars have been detected in multiple environments (Jurcsik et al. 2015; Soszyński et al. 2016) and appear to be less common than classical RRd stars, overall. Anomalous RRd stars often display indications of long-term amplitude, period, and phase modulation (see e.g., Soszyński et al. 2014; Smolec et al. 2015; Netzel 2022), the so-called Blazhko effect (Blazhko 1907) (which has been observed among different RRL types; see e.g., Catelan & Smith 2015, and references therein), and are characterized by fundamental modes that are more dominant than their first overtones.

As pointed out by Soszyński et al. (2019), the incident rate of double-mode RRLs displays indications of a strong function of metallicity (see e.g., Soszyński et al. 2014, 2016; Jurcsik et al. 2015; Varma & Ngeow 2024).

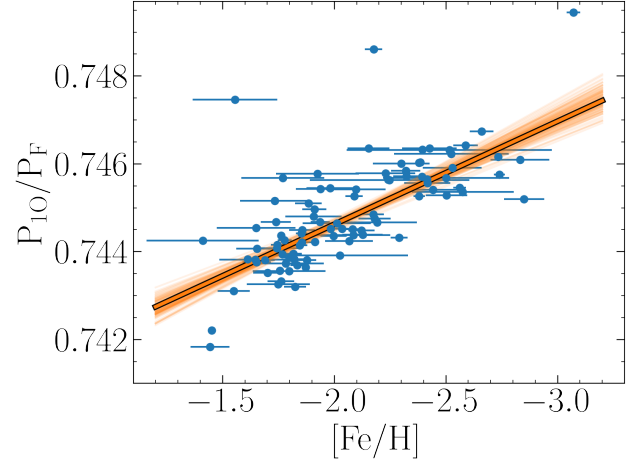


**Figure 9.** Period ratio as a function of  $[\text{Fe}/\text{H}]$  for the DESI Y1 RRd stars, fit with a linear function. In addition to the curve obtained from the median of the linear model parameters’ posterior distributions, 100 curves drawn from the MCMC chains are shown to visualize the variation of the parameters. In this figure, the metallicity is shown decreasing from left to right for a direct comparison with Figure 9 in Braga et al. (2022).

Moreover, the iron abundance of RRd stars plays a role in the position of these stars in the Petersen diagram, as suggested by previous studies (e.g., Bono et al. 1996; Popielski et al. 2000) and recently empirically characterized by Braga et al. (2022), Chen et al. (2023), and Nemec et al. (2024). Here, we take advantage of the sizable sample of field RRd stars observed by DESI in Y1 (107 stars) to further investigate this dependency.

Figure 8 shows the Petersen diagram for the RRd stars in our sample. A metallicity gradient along the canonical sequence is clearly seen in this figure, with the more metal rich RRd stars at present at low  $P_{10}/P_{\text{F}}$  ( $\lesssim 0.744$ , or  $P_{\text{F}} < 0.5$  d), and the more metal poor stars displaying higher period ratios ( $\gtrsim 0.745$ ) with longer fundamental periods. Additionally, the figure shows that at least seven anomalous RRd stars lie below the canonical RRd sequence (with  $0.725 < P_{10}/P_{\text{F}} < 0.735$ ), and at least three lie above it (with  $P_{10}/P_{\text{F}} > 0.747$ ). For all of the anomalous RRd stars, our measured  $[\text{Fe}/\text{H}]$  is  $> -1.77$  dex, and half of them exhibit GSE-like chemodynamics (with probabilities  $p_{\text{GSE}} > 0.5$ ). In contrast, the fraction of classical RRd stars likely associated with GSE ( $p_{\text{GSE}} > 0.5$ ) is only 18%. We note that all of the observed  $[\text{Fe}/\text{H}]$  of our RRd sample, including those of anomalous RRd stars, lies within the expectations from theoretical models (from stellar mass-metallicity-period ratio correlations; see e.g., Marconi et al. 2015). It is im-

portant to mention that the  $[\text{Fe}/\text{H}]$  distribution of these anomalous RRd stars is significantly narrower than that of classical RRd stars ( $-1.77 < [\text{Fe}/\text{H}] < -1.36$  dex vs.  $-2.85 < [\text{Fe}/\text{H}] < -1.41$  dex, respectively). Using the well-defined mass-metallicity-period-ratio relation from Marconi et al. (2015), we can constrain the mass of our sample of canonical RRd stars to  $> 0.69 M_{\odot}$  (our sample extends to lower metallicities than those in their models), and the mass of the anomalous RRd subsample to the range  $0.68\text{-}0.77 M_{\odot}$ .

In Figure 9, we display the period ratios of our RRd stars as a function of  $[\text{Fe}/\text{H}]$ . The figure shows a relatively large scatter of  $P_{10}/P_F$  at a given  $[\text{Fe}/\text{H}]$ , of  $\sim 0.0015$ . We note that, as discussed by Popielski et al. (2000) and Marconi et al. (2015), the scatter in period ratio at a given  $[\text{Fe}/\text{H}]$  could be explained by the spread in stellar mass of RRd stars, and that more massive RRd stars are expected to show larger period ratios at a given fundamental-mode period (see e.g., Alcock et al. 1999; Kovács & Walker 1999; Soszyński et al. 2011). Using the Python package `emcee`, we look for the best fitting parameters for the period ratio- $[\text{Fe}/\text{H}]$  relation for classical RRd stars adopting a linear dependence. We use `scipy`'s `optimize` module to find initial guesses for `emcee`, maximizing the likelihood of the parameters to be fitted and adopting the results from Braga et al. (2022) as initial guesses for the routine. For `emcee`, we adopt uniform priors, namely  $\mathcal{U}(0, 2)$  and  $\mathcal{U}(-0.5, 0.5)$  for the zeropoint and the slope of the linear model, respectively. From this analysis, we obtain

$$P_{10}/P_F = 0.7399^{+0.0004}_{-0.0004} - 0.0023^{+0.0002}_{-0.0002} [\text{Fe}/\text{H}] \quad (3)$$

From this equation, we note the remarkable agreement with the results from Braga et al. (2022),  $P_{10}/P_F = (0.7404 \pm 0.0007) - (0.0025 \pm 0.0004) [\text{Fe}/\text{H}]$ , particularly considering the different approaches used to derive  $[\text{Fe}/\text{H}]$  (in their case, based on the newest calibration of the  $\Delta S$  method; Crestani et al. 2021a). We note, however, that the quality of the fits can be largely affected by the presence or absence of RRd stars with measured  $[\text{Fe}/\text{H}] < -2.7$  and  $> -1.7$ . Thus, larger samples of RRd stars in the metal-poor and metal-rich end of the  $[\text{Fe}/\text{H}]$  distribution are likely required to draw firmer conclusions on the validity of this model to describe the data.

## 5. THE EDGES OF THE RR LYRAE INSTABILITY STRIP

Since RRLs occur in a specific region of the HR diagram (where the horizontal branch crosses the instability strip), characterizing the morphology of their luminosity and  $T_{\text{eff}}$  distribution in this region, both empirically

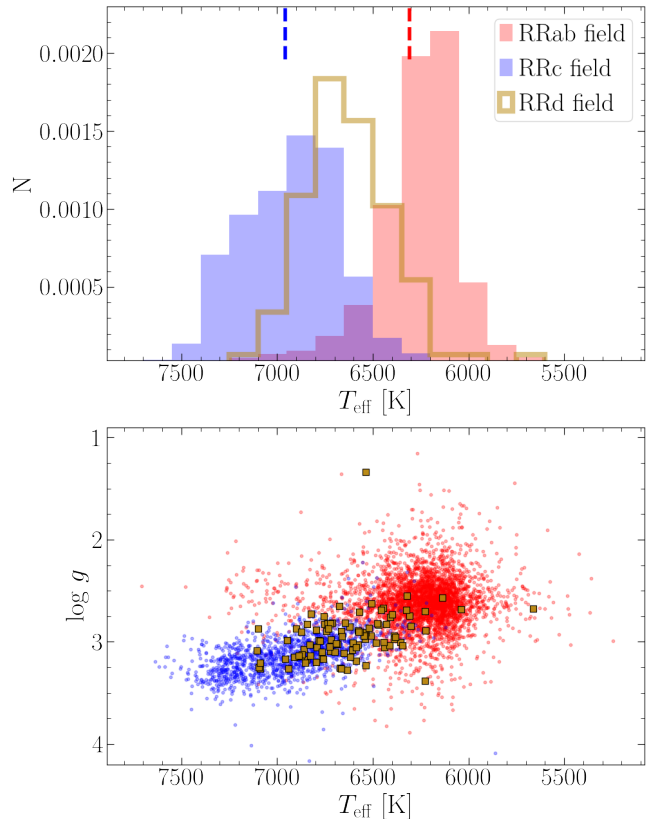


**Figure 10.** *Top:* Normalized distribution of (systemic) effective temperatures for the different RRL sub-types in our field sample, in  $T_{\text{eff}}$  bins of 150 K. Vertical dashed lines depict the median of the for each sub-type. The 5th and 95th percentiles of the  $T_{\text{eff}}$  of RRab and RRc variables reflect empirical instability strip cold and hot boundaries for field RRLs of 5955 and 7366 K, respectively. *Bottom:* Kiel diagram of the DESI field RRLs. This figure shows that the bulk of the RRab and RRc distributions occupy distinct regions of the  $T_{\text{eff}}$  vs.  $\log g$  space, with the limit lying close to  $T_{\text{eff}} \sim 6500$  K and  $\log g \sim 3$ . In both panels, the bulk of the distribution of double mode pulsators is located between RRab and RRc stars in  $T_{\text{eff}}$ . We note the presence of an outlier in the RRd distribution, resulting from an inaccurate model fit by the RVS pipeline (its  $\log g$  and  $T_{\text{eff}}$  measured by DESI's SP pipeline are 3.2 and 6700 K, respectively, consistent with the rest of the RRd distribution).

and theoretically, plays an important role in our understanding of stellar evolution and the use of RRLs as population tracers. Indeed, the position of the blue and red edges of the RR Lyrae instability strip provide key insight on the theory of stellar pulsations, as specific physical conditions are required to drive pulsations in the stellar interiors through their heat mechanism, that is, the  $\kappa$  and  $\gamma$  mechanisms (see e.g., Bono & Stellingwerf 1994). The blue edge's location is relevant since,

if a star is too hot, a partial ionization zone of H or He (the responsible of the  $\kappa$  and  $\gamma$  mechanism-driven pulsations) might not be present in the star, or might be located too far out in the star to trigger or maintain pulsations (Iben 1971; Catelan & Smith 2015). Similarly, the position of the red edge is important to understand the limit in temperature in which stellar convection and its efficient transport of energy quenches the pulsations (e.g., Schatzman 1956; Xiong 1982; Bono et al. 1995a). However, no large scale empirical study of the topology of the instability strip using RRLs (especially with homogeneously-derived spectroscopic properties) has been performed to date.

The rich and homogeneous DESI dataset offers an excellent opportunity to constrain empirically, for the first time using a large number of stars and pulsation-corrected  $T_{\text{eff}}$ , the behavior of the hot and cold ends of the RRL instability strip, and their dependence on  $[\text{Fe}/\text{H}]$ . We note that it is expected that the colors (and temperatures) of RRLs during a considerable portion of their pulsation cycle (e.g., prior minimum light for RRab) lie outside the instability strip (see e.g., For et al. 2011). Therefore, the observation phase of the stars must be considered when estimating the instability strip boundaries. Here, we use the RRL effective temperatures derived in M25 to study these boundaries. These estimates of the stars' mean  $T_{\text{eff}}$  are computed mainly from single epoch spectra, accounting for cyclic variations by adopting  $T_{\text{eff}}$  curve corrections. Additionally, we remove stars with  $T_{\text{eff}}$  smaller than 4800 K and hotter than 8250 K, as we consider them outliers of the  $T_{\text{eff}}$  distribution.

Figure 10 shows the distribution of mean effective temperatures for the 5,438 halo field RRLs in our sample with reliable temperature estimations, separated by RRL type. The median of the  $T_{\text{eff}}$  distributions shown in the figure is  $6224^{+181}_{-182}$  K for RRab,  $6931^{+293}_{-245}$  K for RRC, and  $6676^{+227}_{-224}$  K for RRd variables. For a comparison with the  $T_{\text{eff}}$  of RRLs in a more metal-poor population, we show in Figure 11 the  $T_{\text{eff}}$  distribution of the 59 RRLs in Draco ( $[\text{Fe}/\text{H}] \sim -2.0$  dex), where the median  $T_{\text{eff}}$  of the RRab and RRC is  $6187^{+248}_{-232}$  and  $6735^{+290}_{-261}$  K, respectively. Thus, in these plots we can see the effects of metallicity in the shape and position of the distributions, and therefore the boundaries of the instability strip. From these distributions, we define the blue edge of the RRL instability strip to be the temperature corresponding to the 95th percentile of the RRC distribution, and the red edge as the 5th percentile limit of the RRab distribution. These limits represent the temperature range out of which the number of stars becomes comparatively negligible. According to these definitions

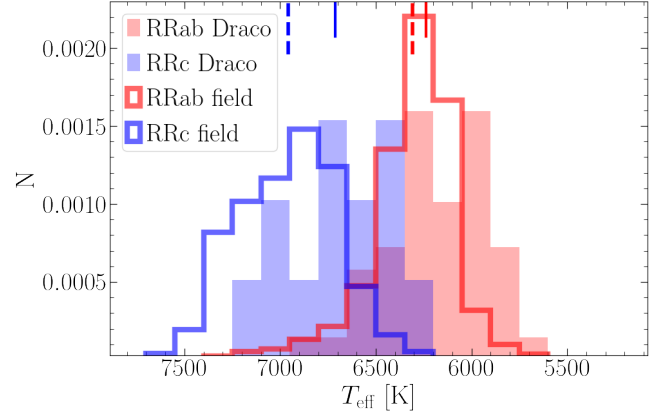


**Figure 11.** Same as Figure 10 (top) but for the 59 RRLs in Draco (filled histograms). Unfilled histograms are used to show the  $T_{\text{eff}}$  distribution of RRab and RRc in our field sample. Solid vertical lines represent the median of the distributions for Draco's RRLs, whereas the values from the field sample are shown with dashed lines (as shown in Figure 10). The lower median  $T_{\text{eff}}$  of the RRab and RRc in Draco ( $6187^{+248}_{-232}$  and  $6735^{+290}_{-261}$  K, respectively) as compared with those from the field sample ( $6228^{+181}_{-182}$  and  $6931^{+293}_{-245}$  K) indicate the difference in the  $T_{\text{eff}}$  distribution shape as a function of metallicity.

and considering the entire sample irrespective of their metallicities, we find that the boundaries of the instability strip for field RRLs at the cold and hot boundaries are 5963 and 7371 K, respectively. For the Draco-only sample, these values are 5808 and 7101 K. A more detailed inspection of the variation of the instability strip edges with metallicity is provided in Section 5.1, including a comparison with previous results.

### 5.1. The boundaries of the instability strip and $[\text{Fe}/\text{H}]$

To quantify the dependence of the boundaries of the instability strip on metallicity, we followed the methodology described in Section 3.1, this time using  $T_{\text{eff}}$  instead of periods and amplitudes of pulsation. In other words, we split our sample of RRLs in  $[\text{Fe}/\text{H}]$  bins containing the same number of stars (in the  $[\text{Fe}/\text{H}]$  range  $[-2.79, -1.19]$  dex), and computed percentile statistics for  $T_{\text{eff}}$  in each bin. We note that, for the red edge (RE) and blue edge (BE) based on these distributions, defined as the  $1\sigma$  limits per bin (16th and 84th percentiles of the RRab and RRC  $T_{\text{eff}}$  distribution, respectively), we find linear trends in the  $[\text{Fe}/\text{H}]$  range explored, hence we fit linear relations for them. We repeated this for the  $2\sigma$  limits (5th and 95th percentiles of the RRab and RRC  $T_{\text{eff}}$  distribution). The results of this exercise can be expressed as

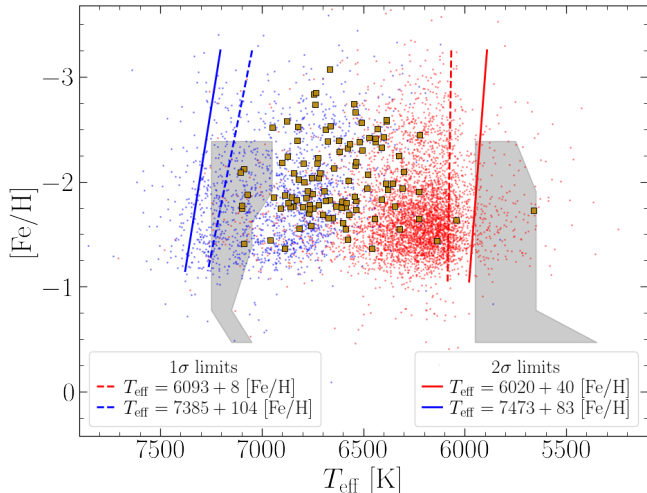


**Figure 12.** Similar to Figure 4, but depicting the mean  $T_{\text{eff}}$  for the stars in our sample against their RVS iron abundances. In this diagram, RRc stars are located in the hotter side of the RRL  $T_{\text{eff}}$  distribution (blue markers), whereas RRab (red markers) lie toward the cooler edge of the instability strip. Brown markers represent RRd stars, which lie predominantly in the region between RRab and RRc. The data is split in metallicity bins containing equal number of stars (separately for RRab and RRc), in the  $[\text{Fe}/\text{H}]$  range  $[-2.79, -1.19]$  dex. Linear fits to the [16th, 84th] and [5th, 95th] running percentiles are displayed with dashed and filled lines (corresponding to their type colors). The theoretical predictions for the edges of the RRL instability strip provided by Marconi et al. (2015) for different combinations of stellar masses, luminosities, and chemical abundances are shown as shaded regions. The leftmost borders of these regions represent the instability strip edges for the ZAHB and masses between  $0.54\text{-}0.80 M_{\odot}$ .

$$\begin{aligned} T_{\text{eff}} (\text{RE}) [\text{K}] &= 6093 (\pm 15) + 8 (\pm 9) [\text{Fe}/\text{H}], \\ T_{\text{eff}} (\text{BE}) [\text{K}] &= 7385 (\pm 45) + 104 (\pm 24) [\text{Fe}/\text{H}] \end{aligned} \quad (4)$$

for the  $1\sigma$  limits, and

$$\begin{aligned} T_{\text{eff}} (\text{RE}) [\text{K}] &= 6020 (\pm 47) + 40 (\pm 27) [\text{Fe}/\text{H}], \\ T_{\text{eff}} (\text{BE}) [\text{K}] &= 7473 (\pm 37) + 83 (\pm 20) [\text{Fe}/\text{H}] \end{aligned} \quad (5)$$

for the  $2\sigma$  limits.

Figure 12 depicts these correlations for both RRab and RRc. These equations show that the  $T_{\text{eff}}$  of the instability strip boundaries are mildly correlated with metallicities, with the exception of the RE of the  $1\sigma$  selection, where the correlation is negligible. Based on these definitions of the instability strip boundaries, we would expect the RE to lie somewhere between 5956 K and 6079 K for field stars in the inner halo ( $[\text{Fe}/\text{H}]$

$\sim -1.6$  dex), and between 5940 K and 6076 K for a more metal-poor stellar population ( $[\text{Fe}/\text{H}] \sim -2.0$  dex). Similarly, one would expect a BE in the range [7219, 7340] K for  $[\text{Fe}/\text{H}] \sim -1.6$  dex, and [7177, 7307] K for  $[\text{Fe}/\text{H}] \sim -2.0$  dex.

Marconi et al. (2015) predicted the position of the edges of the instability strip using nonlinear convective hydrodynamical models of RRLs in a broad range in metal abundances ( $Z = 0.0001\text{-}0.02$ ). Figure 12 also shows the region in  $[\text{Fe}/\text{H}]$  vs.  $T_{\text{eff}}$  space covered by the discrete predicted values of the first overtone blue edge and the fundamental red edge of the instability strip, as provided by Marconi et al. (2015) (Table 2 in their work). These values include the instability strip edges at the zero-age horizontal branch (ZAHB) for stellar masses of  $0.54\text{-}0.80 M_{\odot}$  (the leftmost limit of each shaded region in Figure 12; sequence A in their table), and those for a luminosity 0.1 dex brighter than the ZAHB (sequence B), for the luminosity of central He exhaustion (sequence D), and for a 10% less massive and 0.2 dex brighter than the ZAHB model (sequence C). We find a remarkable agreement between the predicted red edge at the ZAHB and our  $2\sigma$  limit in the entire  $[\text{Fe}/\text{H}]$  range of comparison. For the blue edge, the predicted boundary at the ZAHB lies between the  $1\sigma$  and the  $2\sigma$ , with  $T_{\text{eff}}$  consistent with  $1\sigma$  at higher metallicity and with  $2\sigma$  at lower metallicity. We note that our measurements (as characterized by Equation 5, i.e., our  $2\sigma$  limit) are in agreement with the results from Marconi et al. (2015), which predict a roughly constant width (of the order of  $\sim 1300\text{-}1400$  K) among different chemical compositions. In Figure 12, we find that the instability strip as a whole moves towards cooler  $T_{\text{eff}}$  with more metal-poor RRLs, although this trend is less clear at the red end. This tendency is also observable if we consider non-corrected  $T_{\text{eff}}$  from DESI’s RVS or SP pipelines. Interestingly, a similar trend was identified by Luo et al. (2021) using  $\sim 400$  RRab in LAMOST DR6, and previously reported by Sandage (1993). We note that these results contrast the predictions of Marconi et al. (2015) (available down to  $[\text{Fe}/\text{H}] \sim -2.20$  dex) of a shift toward cooler  $T_{\text{eff}}$  with increasing metal content. Potential explanations for this shift include a systematic loss of precision and accuracy for  $[\text{Fe}/\text{H}]$  and/or  $T_{\text{eff}}$  in the very metal-poor regime ( $[\text{Fe}/\text{H}] < -2$  dex) in our data or the unsuitability of the hydrodynamical models considered in this metallicity regime. The discrepancy could also be explained by the relative numbers of post-ZAHB stars at different metallicities or by the lack of sizable samples of RRLs near the blue edge of the fundamental-mode instability strip (which could cause the 5th and 16th percentiles to move towards hot-

**Table 1.** Statistics of the  $T_{\text{eff}}$  distribution of RRab and RRc in ten metallicity bins, each containing the same number of stars ( $N$ ). The columns q1, q5, q16, q50, q84, q95, and q99 correspond to the 1st, 5th, 16th, 50th, 84th, 95th, and 99th percentiles of the  $T_{\text{eff}}$  distributions, respectively.

Type	[Fe/H] range (dex)	q1 (K)	q5 (K)	q16 (K)	q50 (K)	q84 (K)	q95 (K)	q99 (K)
RRab ( $N = 451$ )	$[-2.30, -1.99[$	5666	5954	6066	6250	6466	6698	7156
	$[-1.99, -1.83[$	5732	5948	6066	6203	6445	6751	7008
	$[-1.83, -1.72[$	5709	5975	6081	6234	6432	6631	6907
	$[-1.72, -1.63[$	5740	5950	6085	6225	6438	6745	7078
	$[-1.63, -1.55[$	5803	5993	6094	6237	6452	6677	7061
	$[-1.55, -1.48[$	5755	5952	6083	6211	6430	6659	6916
	$[-1.48, -1.40[$	5834	5985	6078	6223	6434	6760	7185
	$[-1.40, -1.30[$	5719	5967	6076	6229	6429	6651	6892
RRc ( $N = 161$ )	$[-2.56, -2.27[$	6316	6379	6560	6786	7112	7251	7377
	$[-2.27, -2.05[$	6324	6512	6695	6915	7193	7307	7462
	$[-2.05, -1.92[$	6452	6559	6669	6887	7231	7332	7511
	$[-1.92, -1.79[$	6466	6600	6709	6873	7217	7326	7443
	$[-1.79, -1.66[$	6394	6529	6684	6893	7203	7347	7479
	$[-1.66, -1.53[$	6388	6612	6718	6874	7211	7369	7479
	$[-1.53, -1.42[$	6598	6677	6733	6945	7229	7308	7415
	$[-1.42, -1.31[$	6421	6708	6789	6940	7248	7348	7473

ter temperatures) and RRc near the blue edge of the instability strip (idem, but for the 84th and 95th percentiles).

In Table 1, we report percentiles of the  $T_{\text{eff}}$  distributions of RRab and RRc in different [Fe/H] bins (each containing the same number of stars). The trend described above for the boundaries of the instability strip, which is more pronounced for RRc stars, can be deduced from the numbers shown in the table. These numbers do not show a consistent variation of the width of the RRab star  $T_{\text{eff}}$  distribution with [Fe/H], and that is also the case for RRc stars. Moreover, we can infer details about the region that separates the RRab and RRc distributions in  $T_{\text{eff}}$ . For instance, the 95th percentile  $T_{\text{eff}}$  limit of RRab stars across [Fe/H] is most similar to the 16th percentile of RRc stars. In practice, this means that in terms of relative numbers, the region occupied by the hotter end of the RRab distribution contains a high fraction of RRc stars. Figure 12 also shows that the bulk of the RRd  $T_{\text{eff}}$  distribution lies in this region, where the fundamental and the first-overtone modes approach pulsationally stable nonlinear cycles (the so-called ‘‘OR’’ region; see e.g., Marconi et al. 2015).

A number of previous studies have empirically estimated the effective temperature at the red-horizontal branch (RHB) boundary where the onset of convection suppresses stellar pulsations. Preston et al. (2006), for instance, analyzed the temperature distribution of

24 field metal-poor ([Fe/H] < -2 dex) red horizontal-branch stars and six of these stars in the very metal-poor globular cluster M15, combined with globular cluster RRL data, to infer the  $T_{\text{eff}}$  of the fundamental red edge of the metal-poor RRL instability strip of  $\sim 6310 \pm 150$  K. Later, For & Sneden (2010) performed a similar comparison between non-variable HB stars and RRLs in the range  $-2.5 < [\text{Fe}/\text{H}] < -0.8$  and found an RHB boundary at  $\sim 5900$  K, showing that their lower metallicities translate into a lower  $T_{\text{eff}}$  at the red edge of the instability strip than that of Preston et al. (2006), in good agreement with the results of Hansen et al. (2011) using two extremely metal-poor RRLs ([Fe/H] < -2.5). For et al. (2011) used 2300 high-resolution spectra of 11 field RRab stars with  $-2.0 < [\text{Fe}/\text{H}] < -1.0$  to estimate the position of the instability strip red-edge to lie at  $6280 \pm 30$  K, similar to the results of Preston et al. (2006), although a more metal-rich sample was used in the latter case. Based on large number statistics, we estimate a RHB boundary in the range [5956, 6079] K for inner halo field stars and [5940, 6076] K for [Fe/H]  $\sim 2.0$  dex. Thus, our results are more consistent with those of For & Sneden (2010) and Hansen et al. (2011). This is also the case for our RHB limit estimation from our Draco-only sample.

Lastly, we note in passing that Gillet (2013) recognized that RRab exhibiting Blazhko modulation are preferentially located near the blue-edge of the RRL

fundamental-mode instability strip (as opposed to non-Blazhko RRab often found closer to the redder edge of fundamental-mode pulsation). We identify the investigation of the location of Blazhko vs non-Blazhko RRab in the HR diagram as a direct application of the DESI Y1 RRL catalog, but a detailed analysis of this science case is beyond the scope of this paper.

## 6. METAL-RICH RRL CANDIDATES

The traditional formation scenario for RRLs involves single-star evolution, where the fraction of horizontal branch stars that cross the instability strip (therefore, their overall pulsation properties) depend on their metallicity, initial mass, and wind mass-loss during the red giant phase. This single evolution channel produces RRLs that are old ( $> 10$  Gyr) and metal-poor ( $[\text{Fe}/\text{H}] < -1$  dex) Population II stars, which are those predominantly observed in the Galaxy. An additional formation channel involving binary system evolution was recently discussed by [Bobrick et al. \(2024\)](#) based on stellar evolution simulations from the Modules for Experiments in Stellar Astrophysics (MESA) code ([Paxton et al. 2011, 2019](#)). In this scenario, a horizontal branch star that falls in the instability strip can be produced when one of the stars in the system strips material from its red giant branch companion (the RRL progenitor). The likelihood of this happening depends on the amount of stripped material, among other factors. By performing a chemodynamical study of *Gaia* DR3 RRLs, [Bobrick et al. \(2024\)](#) found that  $\sim 10\%$  of the Galactic RRLs and the majority of those with observed high metallicities ( $[\text{Fe}/\text{H}] \geq -1.0$ , e.g., in the Solar neighborhood) can be formed in binary systems. Moreover, these authors predicted that all metal-rich RRLs have an A, F, G, or K-type companion with an orbital period  $> 1,000$  d, and that approximately one of every 1,000 RRLs can be a product of binary formation. We note, however, that to the best of our knowledge no strong empirical evidence has been found to support this formation scenario.

Metal-rich RRLs that were not formed via the canonical single evolution channel challenge our understanding of stellar evolution, binarity, and the formation of our Galaxy. These stars have been observed in the Galaxy with chemo-dynamical properties (iron abundances, spatial distribution, and kinematics) consistent with those of thin disk stars (see e.g., [Liu et al. 2013](#); [Marsakov et al. 2019](#); [Prudil et al. 2020](#); [Zinn et al. 2020](#); [Crestani et al. 2021b](#); [Iorio & Belokurov 2021](#)). The (theoretical) scenario that describes the pulsational and evolutionary properties of metal-rich RRLs requires their progenitors to undergo substantial mass loss during their ascent to the red giant branch ([Bono et al.](#)

[1997a,b](#)), induced, for instance, by shock wave winds, radiation pressure, and/or high rotation rates (see e.g., [D’Cruz et al. 1996](#)). The binary system formation scenario provides a means for this considerable mass loss and also allows RRLs to be formed at young ages (anywhere between 1-10 Gyr old), challenging the traditional view of RRLs as exclusively old stellar populations. Indeed, the age-metallicity relation obtained by [Bobrick et al. \(2024\)](#) for binaries in their MESA simulation (see their Figure 6) shows that, with high confidence, the metal-rich tail of the RRL distribution ( $[\text{Fe}/\text{H}] > -0.5$ ) traces young populations (younger than 5 Gyr). This is supported by the recent findings of [Zhang et al. \(2025\)](#), who reported that RRLs with  $[\text{Fe}/\text{H}] > -0.5$  dex display kinematics consistent with a population significantly younger than typically assumed for RRLs. Although RRLs in binary systems have been well studied in the past (see e.g., [Smolec et al. 2013](#); [Hajdu et al. 2015](#); [Kervella et al. 2019](#); [Karczmarek et al. 2017](#); [Prudil et al. 2019](#)), the identification of sizable (confirmed) samples of metal rich (and young) RRLs has been hindered by the need for large spectroscopic information of RRLs samples in different regions of the Galaxy and the requirements for the confirmation of their binary status. Here, we discuss potential metal-rich candidates in the DESI Y1 RRL sample.

### 6.1. Selection and kinematics of metal-rich candidates

[Bobrick et al. \(2024\)](#) showed that regions containing metal-rich and young stars in dynamically cold orbits, like the thin disk, are good environments for the identification of metal-rich and young RRLs. Thus, identifying metal-rich candidates in a survey that does not focus on these regions, like DESI, might provide useful constraints on the nature of binary star evolution, and Galactic dynamics. We employ the observed properties of DESI’s metal-rich RRLs (systemic velocities, heliocentric distances, and proper motions) to investigate the nature of their kinematics and trace their origins back in time.

We consider stars with  $[\text{Fe}/\text{H}] \geq -0.5$  dex in the DESI RRL sample as candidate metal rich RRL. According to this criterion, nine stars fall into the metal-rich candidate category when using RVS-based iron abundances ( $[\text{Fe}/\text{H}]_{\text{RVS}}$ ), and a total of 63 RRLs exhibit  $[\text{Fe}/\text{H}] > -0.5$  dex from either of the three methods used to determine metallicity for DESI’s RRLs. Of the nine RRLs with  $[\text{Fe}/\text{H}]_{\text{RVS}} > -0.5$  dex, one star (with *Gaia* SOURCE\_ID 1209496845350566656) displays almost no clear absorption lines in its spectrum (its S/N is  $< 3$  at wavelengths  $< 5500$  K), with the exception of the calcium triplet region (between 8498 and

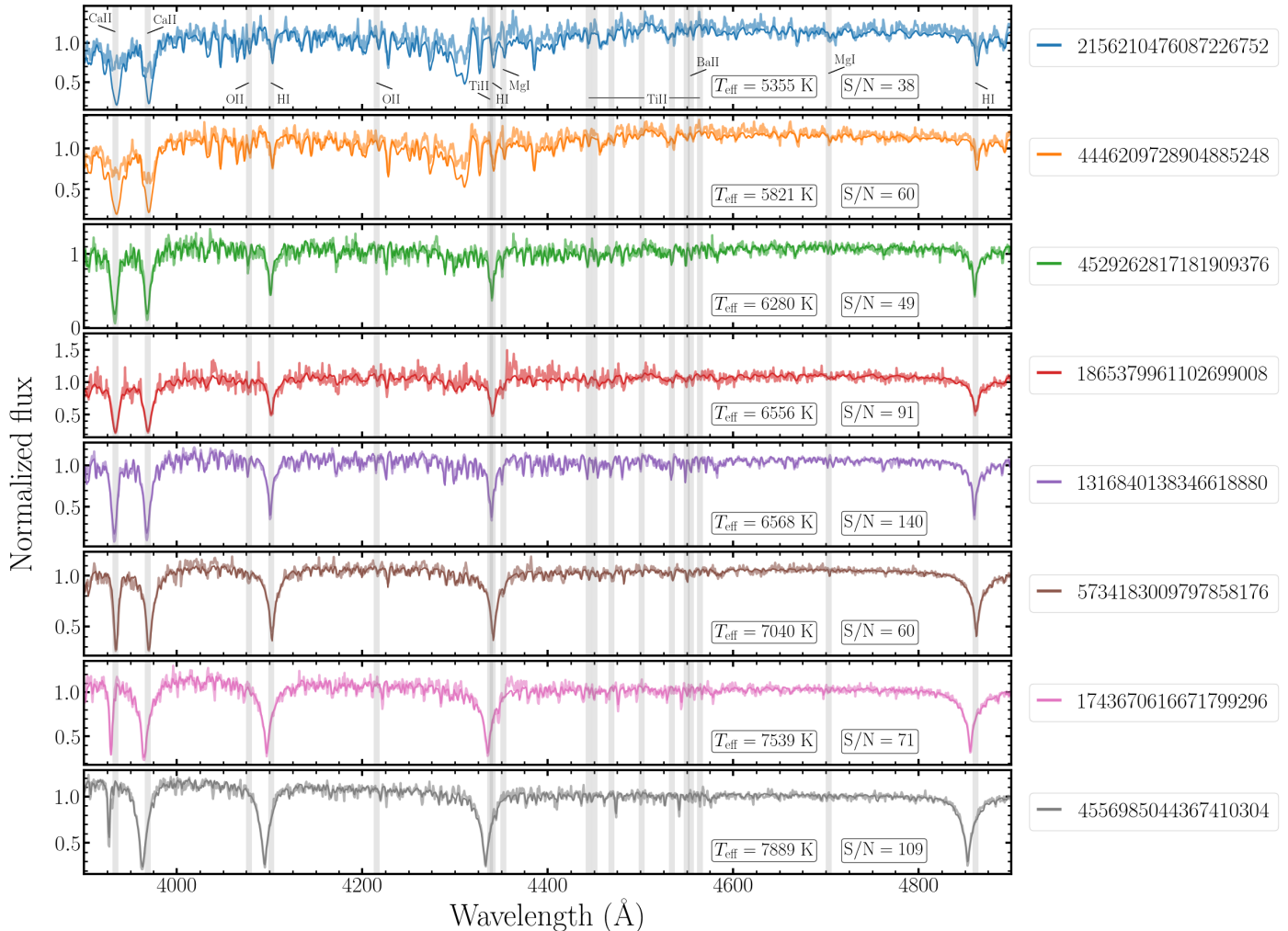


**Figure 13.** Spectra of the eight RRLs in the DESI catalog that display  $[\text{Fe}/\text{H}] > -0.5$  dex (from the RVS pipeline), which are described in Section 6. The observed spectra are depicted with thinner and more transparent lines, whereas the best-fitting RVSpec models are shown with thicker lines. The region displayed contains three absorption lines in the Balmer series ( $\text{H}_\beta$ ,  $\text{H}_\gamma$ ,  $\text{H}_\delta$ ), in addition to calcium (Ca II H and Ca II K) and lines used by Medina et al. (2023). The signal-to-noise ratio of the spectra in the blue arm of the detector is shown as a reference.

8662 Å), where  $\text{S/N} \sim 25$ . A tenth star, classified in *Gaia* as an RRc star (1736044064723548160) with low BEST\_CLASS\_SCORE (previously discussed as a contaminant in our SASP sample; see Section 3.2), also displays  $[\text{Fe}/\text{H}]_{\text{RVS}} > -0.5$  dex. For this star, we find large proper motions with small uncertainties (with proper motions of  $-12.39 \pm 0.79$  and  $-21.24 \pm 0.83 \text{ mas yr}^{-1}$  in right ascension and declination) for its distance ( $d_{\text{H}} = 54.4 \pm 1.0 \text{ kpc}$ ), in addition to a high eccentricity ( $\sim 0.99$ ) and negative parallax ( $-2.60 \pm 0.9 \text{ mas yr}^{-1}$ ). Hence, this star is most likely a contaminant in the sample (i.e., not an RRL). The spectra of the eight remaining stars, as well as their best-fitting models (from the RVS pipeline), are displayed in Figure 13, and their main properties are reported in Table 2.

Of the eight stars with good spectra shown in Figure 13, two show  $[\text{Fe}/\text{H}]$  metallicities from DESI’s SP pipeline also consistent with the  $> -0.5$  dex threshold (4556985044367410304 and 4529262817181909376), and two show  $\Delta\text{S}$ -method metallicities larger than  $-0.5$  dex (4529262817181909376 and 1865379961102699008). Of these, the star 4529262817181909376 shows  $[\text{Fe}/\text{H}] > -0.5$  dex from all three methods. We note that for two RRAb stars (those with the lowest  $T_{\text{eff}}$ , 2156210476087226752 and 4446209728904885248) the best model from the RVS pipeline does not provide a good fit to the most prominent lines shown in Figure 13, and the measured  $[\text{Fe}/\text{H}]$  is mostly influenced by the presence of metallic lines in the reddest part of the spectra (namely, the calcium triplet region). Moreover, for

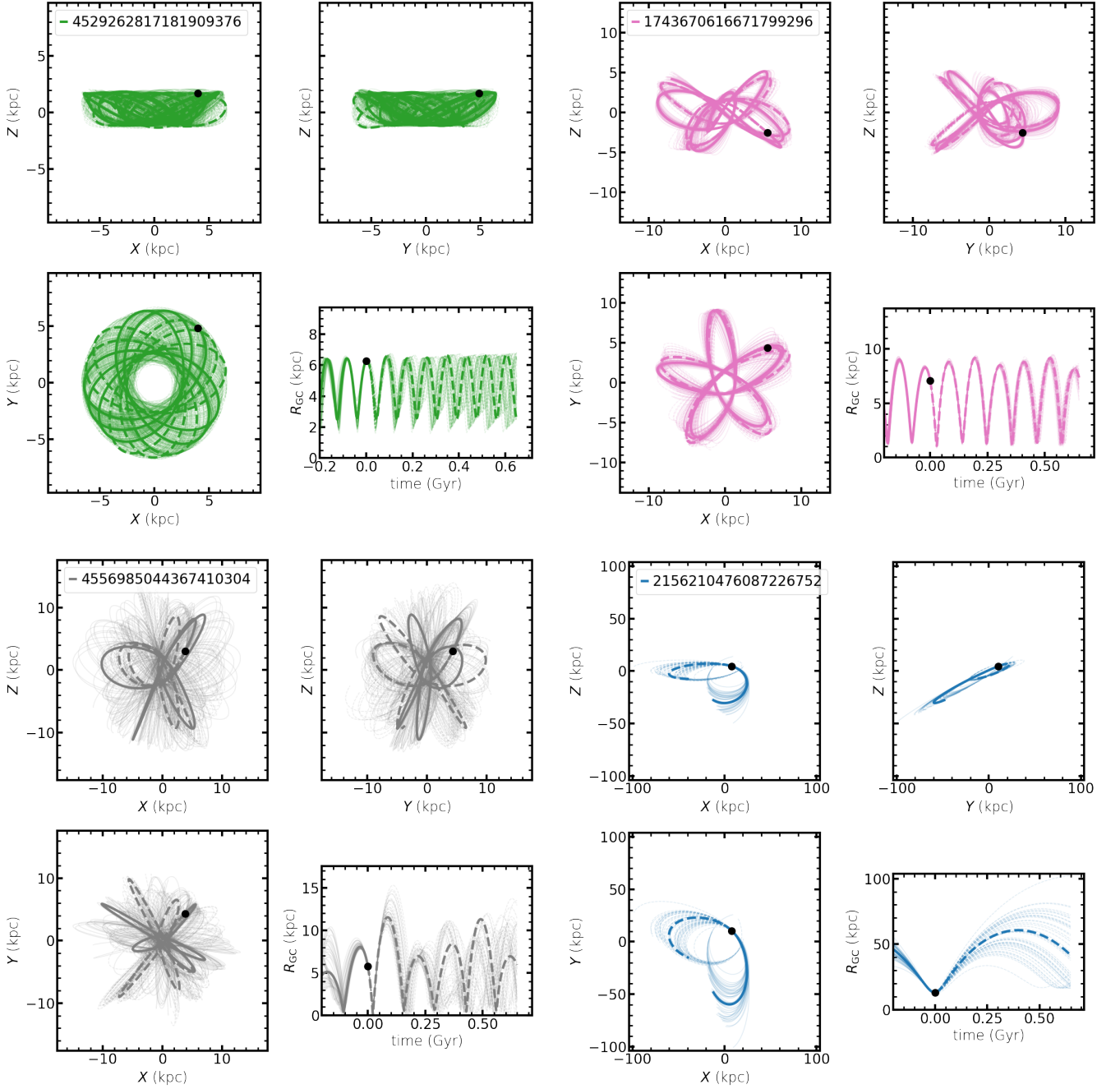


**Figure 14.** Orbits of four of the metal-rich candidates discussed in Section 6, in Galactocentric Cartesian coordinates ( $X$ ,  $Y$ , and  $Z$ ) and Galactocentric radius ( $R_{GC}$ ), integrated for 0.65 Gyr. In each panel, a solid line is used to represent the stars' orbits integrated backwards in time, and their inferred future trajectories are shown with dashed lines. These panels also depict a fraction of the orbits computed for the determination of the stars' orbital parameters (10%) with transparent lines. The two sets of panels on top are two examples of stars with disk-like kinematics, corresponding to the stars 4529262817181909376 and 1743670616671799296. We also show the orbit of a metal-rich candidates with signs of halo kinematics (4556985044367410304 and 2156210476087226752).

these two stars the  $[\text{Fe}/\text{H}]$  measured by the SP pipeline and the  $\Delta S$  method are largely inconsistent with those from RVS (as shown in Table 2). Thus, we flag the high  $[\text{Fe}/\text{H}]$  status of these stars as tentative.

As discussed by Bobrick et al. (2024), although metallicity is the main discriminator between single and binary evolution-made RRLs, the detection of their binary companions is a confirmation of the latter. Hints of binarity in RRLs (i.e. evidence of an unseen companion) are typically inferred from the study of the observed minus calculated time of maximum brightness (O-C diagram), which is computed adopting a fixed period and known light curve ephemeris (in this case, a known time of maximum brightness). Indeed, the change in distance between the observer and the RRL in a binary system over its motion around the center of mass of the system (the light-travel time effect Irwin 1952, 1959) induces a modulation of the light curves and therefore a deviation from the expected time of maximum brightness (Sterken 2005). Thus, conducting studies of the O-C diagram of RRLs requires light curves spanning several years to measure cyclic period variations (see e.g., Liška et al. 2016; Prudil et al. 2019; Hajdu et al. 2021; Abdollahi et al. 2025). We note in passing that for this analysis we do not make special considerations for RRLs potentially exhibiting signatures of Blazhko effect. We advocate for a high-resolution spectroscopic follow up to confirm the metal-rich status of these stars, and a detailed analysis of their long-term variability to study indications of binary companions (which is beyond the scope of this work), e.g., by combining data from the Zwicky Transient Facility (ZTF; Bellm 2014; Bellm et al. 2019), the Catalina Real-Time Transient Survey (CRTS; Drake et al. 2009, 2017), and the ASAS-SN catalogue of variable stars (ASASSN; Jayasinghe et al. 2018, 2020).

The orbital parameters of our metal-rich candidates, derived from our GALPY integrations, are shown in Table 3. Specifically, the table shows their galactocentric distances ( $R_{\text{GC}}$ ), total galactocentric velocities ( $V$ ), energies ( $E$ ), pericentric and apocentric distances of their orbits ( $r_{\text{peri}}$  and  $r_{\text{apo}}$ , respectively), and the eccentricity of their orbits ( $e$ ).

Based on the observed orbital properties of our sample, we identify four of the RRLs with  $[\text{Fe}/\text{H}] > -0.5$  dex exhibiting disk-like kinematics (two thin disk and two thick disk), and four with halo-like orbits. The integrated orbits of the stars show a variety of shapes, with patterns that vary from case to case, and traits that include symmetric and asymmetric orbits, short and long orbital periods, among other properties. Figure 14 shows the orbital histories of four of these stars, including 10% of the orbits generated to compute the

orbital parameters and their uncertainties. This figure shows the orbits of two stars that are mostly constrained to the disk region (at  $Z < 2$  kpc) and two that reach larger apocentric distances. Among the latter, 4556985044367410304 displays a highly eccentric orbit that reaches  $Z \sim 10$  kpc, with a pericenter of  $0.5_{-0.2}^{+0.4}$  kpc and an apocenter of  $13.8_{-1.9}^{+3.2}$  kpc. For the second halo-like star, 2156210476087226752, the integrated orbit suggests that it recently reached its pericenter (with  $r_{\text{peri}} = 16.7_{-0.4}^{+0.5}$  kpc), and an apocenter of  $\sim 50$  kpc. We note, however, that this RRL corresponds to one of the stars with a poor RVS model fit in the blue region of its spectrum (as discussed earlier in this section). If confirmed, the high metallicity of these stars and their observed parameters might provide hints of their origin, e.g., as indications of a dynamical ejection from the disk or through constraints on the nature of their formation (and potential association with binary companions).

In Figure 7, the energy and vertical angular momentum of our sample is displayed, highlighting the position of the metal-rich candidates. The figure shows that these stars exhibit orbits that are predominantly prograde, consistent with their classification as disk-like stars. Indeed, the metal-rich candidates appear kinematically distinct to the bulk of the population (displaying radial orbits), in a region dominated by stars associated with the GSE merger event. The position of the RRL with discrepant  $[\text{Fe}/\text{H}]$  measurements from different methods and large apocenter described above (2156210476087226752) in this diagram appears as an outlier of the overall distribution of metal-rich candidates, slightly below the  $E \sim 0 \text{ km}^2 \text{ s}^{-2}$  limit.

## 7. SUMMARY AND CONCLUSIONS

The first year of operation of the Dark Energy Spectroscopic Instrument (DESI) Milky Way Survey provides one of the largest homogeneous samples of RR Lyrae stars (RRLs) available to date to investigate, empirically, existing correlations between their metallicities and their general physical properties. To this end, we used the 6,240 RRLs observed by DESI, with over 12,000 single-epoch observations and spectroscopic properties ( $[\text{Fe}/\text{H}]$ ,  $T_{\text{eff}}$ ) reported by Medina et al. (2025), combined with the pulsating properties reported in the *Gaia* DR3 RRL catalog. The DESI RRL catalog is composed of field stars, and stars associated with known globular clusters, dwarf galaxies, and accretion events (most notably, Sagittarius and Gaia-Sausage-Enceladus).

We analyzed the metallicity gradients observed in the period-visual amplitude ( $P - A_V$ ) space (Bailey diagram). For both fundamental and first-overtone mode

**Table 2.** Main properties of the metal-rich candidate RRLs ( $[\text{Fe}/\text{H}]_{\text{RVS}} > -0.5$  dex) in our sample, including their *Gaia* source\_ids, iron abundances, mean signal-to-noise ratio (S/N), heliocentric distance, and proper motions ( $\mu_{\alpha^*}$ ,  $\mu_{\delta}$ ).

ID	Type	Period (d)	$A_V$ (mag)	$[\text{Fe}/\text{H}]_{\text{RVS}}$ (dex)	$[\text{Fe}/\text{H}]_{\text{SP}}$ (dex)	$[\text{Fe}/\text{H}]_{\Delta S}$ (dex)	S/N	$d_H$ (kpc)	$\mu_{\alpha^*}$ (mas yr $^{-1}$ )	$\mu_{\delta}$ (mas yr $^{-1}$ )
2156210476087226752	RRab	0.6629	0.40	$-0.35 \pm 0.04$	-1.63	-	49	$11.4 \pm 0.2$	$-2.34 \pm 0.05$	$-4.81 \pm 0.05$
4446209728904885248	RRab	0.5509	0.39	$-0.46 \pm 0.02$	-1.76	$-2.51 \pm 0.14$	78	$8.6 \pm 0.1$	$-5.36 \pm 0.04$	$1.71 \pm 0.03$
4529262817181909376	RRab	0.4322	1.05	$-0.42 \pm 0.02$	-0.45	$-0.22 \pm 0.07$	62	$6.5 \pm 0.1$	$-2.55 \pm 0.02$	$-4.15 \pm 0.02$
1865379961102699008	RRc	0.3324	0.31	$-0.10 \pm 0.01$	-0.63	$-0.22 \pm 0.14$	109	$2.7 \pm 0.0$	$0.55 \pm 0.01$	$-6.34 \pm 0.01$
1316840138346618880	RRab	0.9292	0.89	$-0.48 \pm 0.01$	-0.54	-	157	$2.2 \pm 0.0$	$-6.26 \pm 0.01$	$-3.83 \pm 0.01$
5734183009797858176	RRc	0.3316	0.13	$-0.49 \pm 0.02$	-0.83	$-0.61 \pm 0.09$	71	$3.5 \pm 0.1$	$1.46 \pm 0.01$	$-2.96 \pm 0.01$
1743670616671799296	RRab	0.4298	1.11	$-0.41 \pm 0.07$	-0.70	$-1.37 \pm 0.06$	77	$5.6 \pm 0.1$	$-5.51 \pm 0.03$	$-6.47 \pm 0.02$
4556985044367410304	RRab	0.3905	1.39	$-0.26 \pm 0.02$	-0.09	$-1.26 \pm 0.21$	113	$6.7 \pm 0.1$	$-0.13 \pm 0.02$	$-10.01 \pm 0.03$

**Table 3.** Orbital parameters of the metal-rich RRL candidates in our sample, integrated for 5 Gyr using GALPY’s *MWPotential2014* and taking into account the perturbation caused by the infall of the LMC.

ID	$R$ (kpc)	$V_{\text{tot}}$ (km s $^{-1}$ )	$E$ (10 $^5$ km $^2$ s $^{-2}$ )	$L$ (10 $^3$ kpc km s $^{-1}$ )	$r_{\text{peri}}$ (kpc)	$r_{\text{apo}}$ (kpc)	$e$
2156210476087226752	$14.2 \pm 0.2$	$389.0^{+20.2}_{-17.9}$	$-0.17^{+0.08}_{-0.07}$	$5.37^{+0.26}_{-0.23}$	$13.8^{+0.2}_{-3.0}$	$69.6^{+10.0}_{-5.1}$	$0.68^{+0.09}_{-0.03}$
4446209728904885248	$16.5 \pm 0.1$	$270.0^{+16.9}_{-13.6}$	$-0.97^{+0.05}_{-0.04}$	$0.18^{+0.11}_{-0.04}$	$0.3^{+0.2}_{-0.1}$	$15.7^{+3.3}_{-2.2}$	$0.97^{+0.01}_{-0.02}$
4529262817181909376	$13.7 \pm 0.1$	$131.6^{+19.2}_{-17.5}$	$-1.25^{+0.03}_{-0.02}$	$0.85^{+0.12}_{-0.11}$	$2.0^{+0.4}_{-0.4}$	$7.3^{+0.6}_{-0.4}$	$0.57^{+0.08}_{-0.07}$
1865379961102699008	$7.3 \pm 0.0$	$191.1^{+6.6}_{-7.5}$	$-1.08^{+0.01}_{-0.01}$	$1.51^{+0.05}_{-0.06}$	$3.6^{+0.7}_{-2.2}$	$9.8^{+1.2}_{-1.0}$	$0.45^{+0.32}_{-0.08}$
1316840138346618880	$7.5 \pm 0.0$	$143.4^{+4.3}_{-3.8}$	$-1.19^{+0.01}_{-0.01}$	$1.02^{+0.03}_{-0.03}$	$2.5^{+0.3}_{-0.4}$	$8.1^{+0.2}_{-0.3}$	$0.53^{+0.06}_{-0.06}$
5734183009797858176	$9.6 \pm 0.1$	$216.1^{+4.1}_{-3.3}$	$-0.89^{+0.01}_{-0.01}$	$1.84^{+0.03}_{-0.02}$	$1.4^{+0.5}_{-0.7}$	$19.6^{+2.1}_{-3.1}$	$0.87^{+0.06}_{-0.06}$
1743670616671799296	$9.8 \pm 0.1$	$166.6^{+2.6}_{-2.6}$	$-1.12^{+0.01}_{-0.01}$	$0.65^{+0.02}_{-0.01}$	$0.5^{+0.3}_{-0.2}$	$10.9^{+0.7}_{-0.6}$	$0.92^{+0.04}_{-0.05}$
4556985044367410304	$10.9 \pm 0.1$	$247.1^{+18.7}_{-12.1}$	$-1.01^{+0.05}_{-0.03}$	$0.72^{+0.12}_{-0.04}$	$0.5^{+0.4}_{-0.2}$	$13.8^{+3.2}_{-1.9}$	$0.94^{+0.03}_{-0.06}$

RRLs, we find evidence of a strong and smooth anticorrelation between logarithmic period and iron abundances. In the case of RRc variables, these anticorrelations are more subtle if their visual amplitudes are considered instead of their periods, and for RRab stars the correlation is much less significant. With this information, we draw conclusions on the Oosterhoff dichotomy, a long-standing problem in modern astrophysics related to the metallicity of Galactic globular clusters and the mean period of the RRLs they contain, with potential implications on our understanding of the formation and evolution of the Milky Way, stellar evolution, and pulsation theory. Our measurements show smooth gradients in  $[\text{Fe}/\text{H}]$  with period, which support the findings of previous works regarding the Oosterhoff dichotomy as being caused by the dearth of intermediate metallicity Galactic globular clusters with sizeable RRL samples (e.g., Fabrizio et al. 2019, 2021). Larger samples of DESI RRLs in globular clusters, e.g., taking advantage of available updated variable star membership to globular clusters (Prudil & Ferro 2024) and large scale surveys will be important to provide additional evidence

for or against this hypothesis, and the connection of the dichotomy with the dual origin of the Galactic halo (see e.g. Luongo et al. 2024).

We identify stars in our catalog that fall into the high-amplitude short-period (HASP) and the small-amplitude short-period (SASP) categories (for RRab and RRc, respectively). Only field stars or stars associated with the Sagittarius stream populate the HASP and SASP regions in the Bailey diagram, and they are not observed in the sample of RRLs in the Draco dwarf galaxy, nor in the rest of dwarf galaxies and globular clusters observed by DESI Y1. This finding, combined with  $[\text{Fe}/\text{H}]$  distributions of HASP and SASP stars (with medians at  $-1.39$  dex and  $-1.30$  dex), is consistent with these stars having formed in massive satellites (with masses  $> 10^9 M_{\odot}$ ; see e.g., Fiorentino et al. 2017) that experienced a fast early chemical enrichment and were subsequently accreted onto the Milky Way halo. We find a sizable subsample of HASPs and SASPs at large distances ( $R_{GC} > 30$  kpc), and advocate for a high-resolution spectroscopic follow up to gain further insight on their chemical abundances and their origin.

We studied the position of the  $\sim 100$  double mode (RRd) field stars in DESI Y1 in the period ratio vs. fundamental mode period space (Petersen diagram). In this space, which is a powerful diagnostic of the physical properties of old stellar population in stellar systems, we observe a smooth decline in  $[\text{Fe}/\text{H}]$  with increasing fundamental-mode period. Our sample includes several anomalous RRd stars, which exhibit a narrow range of  $[\text{Fe}/\text{H}]$  (between  $-1.8$  and  $-1.4$  dex), in comparison with the  $[\text{Fe}/\text{H}]$  covered by our sample of classical RRd stars (between  $-3.0$  and  $-1.5$  dex). For the latter, we find that the first-overtone to fundamental period ratio is consistent with a linear  $[\text{Fe}/\text{H}]$  dependency. Our derived linear relation is mostly constrained to  $[\text{Fe}/\text{H}]$  between  $-2.7$  and  $-1.7$  dex, and larger RRd samples are required to tests its validity outside this metallicity range. Lastly, using a theoretical mass-metallicity-period-ratio relation from the literature (Marconi et al. 2015), we constrain the mass of our classical RRd sample to  $> 0.69 M_{\odot}$ , and  $0.68\text{-}0.77 M_{\odot}$  for anomalous RRd stars. These measurements highlight the importance of large spectroscopic surveys targeting sizeable samples of RRd stars (and their synergies with theoretical models) on the study of the pulsation properties of RRLs and stellar evolution.

The dependence of the instability strip topology on  $[\text{Fe}/\text{H}]$  provides important insights on the physical conditions required to trigger and maintain stellar pulsations, which influences the use of RRLs as stellar population tracers and the connection of their observed properties (e.g., RRc to RRab ratios in a given system, periods and period changes) with stellar pulsation theory. Based on M25's  $T_{\text{eff}}$  models, we set for the first time empirical constraints on the width of the RRL instability strip using a large spectroscopic dataset and pulsation-corrected  $T_{\text{eff}}$ . For our halo field sample, we find that the red and blue edges of the instability strip lie at around 5963 and 7371 K, respectively (with variations depending on metallicity). We combined RRLs' mean  $T_{\text{eff}}$  with DESI's RVS iron abundances to study the metallicity dependence of the instability strip's shape. We find a roughly constant  $T_{\text{eff}}$  width of 1300-1400 K as a function of  $[\text{Fe}/\text{H}]$  and an overall good agreement between our empirical estimates and those predicted from stellar evolution models (from, e.g., Marconi et al. 2015). However, we observe an instability strip that moves towards cooler  $T_{\text{eff}}$  with declining  $[\text{Fe}/\text{H}]$  (similar to Sandage 1993 and Luo et al. 2021) in particular for its blue end, a trend that is not present in the theoretical estimates from Marconi et al. (2015). This discrepancy could be explained by low number statistics and/or a decrease in precision in the derived  $[\text{Fe}/\text{H}]$  at the very metal-poor end, or the unsuitability of the theoretical estimates at

low metallicities. We also inspect the transition  $T_{\text{eff}}$  region between RRab and RRc stars, where most of the RRd are found, which occurs at  $\sim 6440\text{-}6700$  K (depending on metallicity).

Taking advantage of the large DESI catalog, we inspected the metal-rich end of the RRL  $[\text{Fe}/\text{H}]$  distribution, given the implications of metal-rich RRL formation on stellar evolution theory, binarity, and the use of RRLs as tracers of old stellar populations only. We find eight RRLs with  $[\text{Fe}/\text{H}] > -0.5$  dex, as measured by DESI's main processing pipeline (RVS). Of these stars, two exhibit similarly high metallicities derived by DESI's SP pipeline or the  $\Delta S$  method, and one shows a high metallicity from all three methods. In order to gain insight on the dynamical origin of this subsample, we integrate their orbits using their systemic (center-of-mass) velocities combined with their *Gaia* proper motions. Our results suggest hot disk-like kinematics for half of the stars, whereas the other half displays halo kinematics. Further investigations are required to draw firmer conclusions on the origin of these stars through indications of binarity (one of the configurations that can give rise to metal-rich RRLs; see e.g., Bobrick et al. 2024), and as for the HASP and SASP samples, we advocate for a high-resolution spectroscopic follow up and/or multi-epoch spectra to confirm their observed high metallicities and orbital histories.

The spectroscopic characterization of RRLs to study their formation conditions and their connection with the assembly history of the halo requires large databases containing homogeneously-derived spectroscopic properties, which must take into account their short-period cyclic variations. The next generation of facilities and instruments is delivering (and will deliver) such databases (e.g., the Subaru Prime Focus Spectrograph survey and the 4-metre Multi-Object Spectroscopic Telescope; de Jong et al. 2014; Takada et al. 2014; Tamura et al. 2016; Ibata et al. 2023), including RRLs in all regions of the Galaxy, in globular clusters, and dwarf galaxies. Furthermore, future DESI data releases will significantly increase the observed number of RRLs in the halo, the number of epochs per star, and will improve the variation models used to derive their main properties (e.g., their systemic velocities, effective temperatures, and  $[\text{Fe}/\text{H}]$ ). These large samples of RRLs will also enable the exploration of multiple science cases not covered in this work, including but not limited to, the study of metallicity gradients in globular clusters and dwarf galaxies and the identification of substructures in integrals-of-motion space. Thus, especially when combined with upcoming *Gaia* data releases and their improvements in astrometric precision and accuracy, these

databases will give us the tools to investigate, empirically, multiple aspects of Galaxy evolution, stellar astrophysics, and pulsation theory with unseen detail.

#### DATA AVAILABILITY

The data shown in all the figures of this manuscript will be made available in Zenodo: <https://zenodo.org/me/requests/f8bc0fea-8048-419d-868b-c72f020c8c38>

#### ACKNOWLEDGMENTS

We acknowledge very useful feedback from Márcio Catelan (Pontificia Universidad Católica de Chile), Marcella Marconi (Istituto Nazionale di Astrofisica, INAF, Osservatorio Astronomico di Capodimonte), and Vittorio Braga (Istituto Nazionale di Astrofisica, INAF, Osservatorio Astronomico di Roma). G.E.M. and T.S.L. acknowledge financial support from Natural Sciences and Engineering Research Council of Canada (NSERC) through grant RGPIN-2022-04794. G.E.M. acknowledges support from an Arts & Science Postdoctoral Fellowship and Dunlap Fellowship at the University of Toronto. The Dunlap Institute is funded through an endowment established by the David Dunlap family and the University of Toronto. S.K. acknowledges support from Science & Technology Facilities Council (STFC) (grant ST/Y001001/1).

This material is based upon work supported by the U.S. Department of Energy (DOE), Office of Science, Office of High-Energy Physics, under Contract No. DE-AC02-05CH11231, and by the National Energy Research Scientific Computing Center, a DOE Office of Science User Facility under the same contract. Additional support for DESI was provided by the U.S.

National Science Foundation (NSF), Division of Astronomical Sciences under Contract No. AST-0950945 to the NSF's National Optical-Infrared Astronomy Research Laboratory; the Science and Technology Facilities Council of the United Kingdom; the Gordon and Betty Moore Foundation; the Heising-Simons Foundation; the French Alternative Energies and Atomic Energy Commission (CEA); the National Council of Humanities, Science and Technology of Mexico (CONACYT); the Ministry of Science, Innovation and Universities of Spain (MICIU/AEI/10.13039/501100011033), and by the DESI Member Institutions: <https://www.desi.lbl.gov/collaborating-institutions>. Any opinions, findings, and conclusions or recommendations expressed in this material are those of the author(s) and do not necessarily reflect the views of the U. S. National Science Foundation, the U. S. Department of Energy, or any of the listed funding agencies.

The authors are honored to be permitted to conduct scientific research on Iolkam Du'ag (Kitt Peak), a mountain with particular significance to the Tohono O'odham Nation.

For the purpose of open access, the author has applied a Creative Commons Attribution (CC BY) licence to any Author Accepted Manuscript version arising from this submission.

This research has made use of the SIMBAD database, operated at CDS, Strasbourg, France (Wenger et al. 2000). This research has made use of NASA's Astrophysics Data System Bibliographic Services.

*Software:* `numpy` (van der Walt et al. 2011), `scipy` (Virtanen et al. 2020), `matplotlib` (Hunter 2007), `astropy` (Astropy Collaboration et al. 2013, 2018, 2022), `galpy` (Bovy 2015), `RVSpecFit` (Koposov 2019b), `emcee` (Foreman-Mackey et al. 2013).

#### REFERENCES

- Abdollahi, H., Molnár, L., & Varga, V. 2025, arXiv e-prints, arXiv:2503.01018, doi: [10.48550/arXiv.2503.01018](https://doi.org/10.48550/arXiv.2503.01018)
- Allcock, C., Allsman, R. A., Alves, D., et al. 1999, ApJ, 511, 185, doi: [10.1086/306638](https://doi.org/10.1086/306638)
- Allende Prieto, C., Beers, T. C., Wilhelm, R., et al. 2006, ApJ, 636, 804, doi: [10.1086/498131](https://doi.org/10.1086/498131)
- Allende Prieto, C., Aguado, D. S., González Hernández, J. I., et al. 2023, ApJ, 957, 76, doi: [10.3847/1538-4357/acfa96](https://doi.org/10.3847/1538-4357/acfa96)
- Astropy Collaboration, Robitaille, T. P., Tollerud, E. J., et al. 2013, A&A, 558, A33, doi: [10.1051/0004-6361/201322068](https://doi.org/10.1051/0004-6361/201322068)
- Astropy Collaboration, Price-Whelan, A. M., Sipőcz, B. M., et al. 2018, AJ, 156, 123, doi: [10.3847/1538-3881/aabc4f](https://doi.org/10.3847/1538-3881/aabc4f)
- Astropy Collaboration, Price-Whelan, A. M., Lim, P. L., et al. 2022, ApJ, 935, 167, doi: [10.3847/1538-4357/ac7c74](https://doi.org/10.3847/1538-4357/ac7c74)
- Bailey, S. I., & Pickering, E. C. 1913, Annals of Harvard College Observatory, 78, 1
- Beaton, R. L., Bono, G., Braga, V. F., et al. 2018, SSRv, 214, 113, doi: [10.1007/s11214-018-0542-1](https://doi.org/10.1007/s11214-018-0542-1)
- Bellm, E. 2014, in The Third Hot-wiring the Transient Universe Workshop, ed. P. R. Wozniak, M. J. Graham, A. A. Mahabal, & R. Seaman, 27–33, doi: [10.48550/arXiv.1410.8185](https://doi.org/10.48550/arXiv.1410.8185)

- Bellm, E. C., Kulkarni, S. R., Graham, M. J., et al. 2019, *PASP*, 131, 018002, doi: [10.1088/1538-3873/aaecbe](https://doi.org/10.1088/1538-3873/aaecbe)
- Belokurov, V., Deason, A. J., Koposov, S. E., et al. 2018, *MNRAS*, 477, 1472, doi: [10.1093/mnras/sty615](https://doi.org/10.1093/mnras/sty615)
- Blažko, S. 1907, *Astronomische Nachrichten*, 175, 325, doi: [10.1002/asna.19071752002](https://doi.org/10.1002/asna.19071752002)
- Bobrick, A., Iorio, G., Belokurov, V., et al. 2024, *MNRAS*, 527, 12196, doi: [10.1093/mnras/stad3996](https://doi.org/10.1093/mnras/stad3996)
- Bono, G., Caputo, F., Cassisi, S., Castellani, V., & Marconi, M. 1997a, *ApJ*, 479, 279, doi: [10.1086/303872](https://doi.org/10.1086/303872)
- Bono, G., Caputo, F., Cassisi, S., Incerpi, R., & Marconi, M. 1997b, *ApJ*, 483, 811, doi: [10.1086/304284](https://doi.org/10.1086/304284)
- Bono, G., Caputo, F., Castellani, V., & Marconi, M. 1996, *ApJL*, 471, L33, doi: [10.1086/310320](https://doi.org/10.1086/310320)
- Bono, G., Caputo, F., Castellani, V., et al. 1995a, *ApJ*, 442, 159, doi: [10.1086/175430](https://doi.org/10.1086/175430)
- . 2003, *MNRAS*, 344, 1097, doi: [10.1046/j.1365-8711.2003.06878.x](https://doi.org/10.1046/j.1365-8711.2003.06878.x)
- Bono, G., Caputo, F., & Marconi, M. 1995b, *AJ*, 110, 2365, doi: [10.1086/117694](https://doi.org/10.1086/117694)
- Bono, G., Caputo, F., & Stellingwerf, R. F. 1994, *ApJ*, 423, 294, doi: [10.1086/173806](https://doi.org/10.1086/173806)
- Bono, G., & Stellingwerf, R. F. 1994, *ApJS*, 93, 233, doi: [10.1086/192054](https://doi.org/10.1086/192054)
- Bono, G., Braga, V. F., Crestani, J., et al. 2020, *ApJL*, 896, L15, doi: [10.3847/2041-8213/ab9538](https://doi.org/10.3847/2041-8213/ab9538)
- Bovy, J. 2015, *ApJS*, 216, 29, doi: [10.1088/0067-0049/216/2/29](https://doi.org/10.1088/0067-0049/216/2/29)
- Braga, V. F., Stetson, P. B., Bono, G., et al. 2016, *AJ*, 152, 170, doi: [10.3847/0004-6256/152/6/170](https://doi.org/10.3847/0004-6256/152/6/170)
- Braga, V. F., Fiorentino, G., Bono, G., et al. 2022, *MNRAS*, 517, 5368, doi: [10.1093/mnras/stac2813](https://doi.org/10.1093/mnras/stac2813)
- Byström, A., Koposov, S. E., Lilleengen, S., et al. 2024, *arXiv e-prints*, arXiv:2410.09149, doi: [10.48550/arXiv.2410.09149](https://doi.org/10.48550/arXiv.2410.09149)
- Caputo, F., Castellani, V., & Tornambe, A. 1989, *A&A*, 222, 121
- Caputo, F., Santolamazza, P., & Marconi, M. 1998, *MNRAS*, 293, 364, doi: [10.1046/j.1365-8711.1998.01171.x](https://doi.org/10.1046/j.1365-8711.1998.01171.x)
- Carretta, E., Bragaglia, A., Gratton, R., D’Orazi, V., & Lucatello, S. 2009, *A&A*, 508, 695, doi: [10.1051/0004-6361/200913003](https://doi.org/10.1051/0004-6361/200913003)
- Cassisi, S., Castellani, M., Caputo, F., & Castellani, V. 2004, *A&A*, 426, 641, doi: [10.1051/0004-6361:20041048](https://doi.org/10.1051/0004-6361:20041048)
- Castellani, M., Caputo, F., & Castellani, V. 2003, *A&A*, 410, 871, doi: [10.1051/0004-6361:20031381](https://doi.org/10.1051/0004-6361:20031381)
- Catelan, M. 2009, *Ap&SS*, 320, 261, doi: [10.1007/s10509-009-9987-8](https://doi.org/10.1007/s10509-009-9987-8)
- Catelan, M., Pritzl, B. J., & Smith, H. A. 2004, *ApJS*, 154, 633, doi: [10.1086/422916](https://doi.org/10.1086/422916)
- Catelan, M., & Smith, H. A. 2015, *Pulsating Stars*
- Chen, X., Zhang, J., Wang, S., & Deng, L. 2023, *Nature Astronomy*, 7, 1081, doi: [10.1038/s41550-023-02011-y](https://doi.org/10.1038/s41550-023-02011-y)
- Clementini, G., Ripepi, V., Molinaro, R., et al. 2019, *A&A*, 622, A60, doi: [10.1051/0004-6361/201833374](https://doi.org/10.1051/0004-6361/201833374)
- Clementini, G., Ripepi, V., Garofalo, A., et al. 2023, *A&A*, 674, A18, doi: [10.1051/0004-6361/202243964](https://doi.org/10.1051/0004-6361/202243964)
- Cooper, A. P., Koposov, S. E., Allende Prieto, C., et al. 2023, *ApJ*, 947, 37, doi: [10.3847/1538-4357/acb3c0](https://doi.org/10.3847/1538-4357/acb3c0)
- Cox, A. N., King, D. S., & Hodson, S. W. 1980, *ApJ*, 236, 219, doi: [10.1086/157736](https://doi.org/10.1086/157736)
- Crestani, J., Fabrizio, M., Braga, V. F., et al. 2021a, *ApJ*, 908, 20, doi: [10.3847/1538-4357/abd183](https://doi.org/10.3847/1538-4357/abd183)
- Crestani, J., Braga, V. F., Fabrizio, M., et al. 2021b, *ApJ*, 914, 10, doi: [10.3847/1538-4357/abfa23](https://doi.org/10.3847/1538-4357/abfa23)
- Cruz Reyes, M., Anderson, R. I., Johansson, L., Netzfel, H., & Medaric, Z. 2024, *A&A*, 684, A173, doi: [10.1051/0004-6361/202348961](https://doi.org/10.1051/0004-6361/202348961)
- Cunningham, E. C., Garavito-Camargo, N., Deason, A. J., et al. 2020, *ApJ*, 898, 4, doi: [10.3847/1538-4357/ab9b88](https://doi.org/10.3847/1538-4357/ab9b88)
- D’Cruz, N. L., Dorman, B., Rood, R. T., & O’Connell, R. W. 1996, *ApJ*, 466, 359, doi: [10.1086/177515](https://doi.org/10.1086/177515)
- de Jong, R. S., Barden, S., Bellido-Tirado, O., et al. 2014, in *Society of Photo-Optical Instrumentation Engineers (SPIE) Conference Series*, Vol. 9147, *Ground-based and Airborne Instrumentation for Astronomy V*, ed. S. K. Ramsay, I. S. McLean, & H. Takami, 91470M, doi: [10.1117/12.2055826](https://doi.org/10.1117/12.2055826)
- De Silva, G. M., Freeman, K. C., Bland-Hawthorn, J., et al. 2015, *MNRAS*, 449, 2604, doi: [10.1093/mnras/stv327](https://doi.org/10.1093/mnras/stv327)
- Dékány, I., Grebel, E. K., & Pojmański, G. 2021, *ApJ*, 920, 33, doi: [10.3847/1538-4357/ac106f](https://doi.org/10.3847/1538-4357/ac106f)
- Deng, L.-C., Newberg, H. J., Liu, C., et al. 2012, *Research in Astronomy and Astrophysics*, 12, 735, doi: [10.1088/1674-4527/12/7/003](https://doi.org/10.1088/1674-4527/12/7/003)
- DESI Collaboration, Aghamousa, A., Aguilar, J., et al. 2016a, *arXiv e-prints*, arXiv:1611.00036, doi: [10.48550/arXiv.1611.00036](https://doi.org/10.48550/arXiv.1611.00036)
- . 2016b, *arXiv e-prints*, arXiv:1611.00037, doi: [10.48550/arXiv.1611.00037](https://doi.org/10.48550/arXiv.1611.00037)
- DESI Collaboration, Abareshi, B., Aguilar, J., et al. 2022, *AJ*, 164, 207, doi: [10.3847/1538-3881/ac882b](https://doi.org/10.3847/1538-3881/ac882b)
- DESI Collaboration, Adame, A. G., Aguilar, J., et al. 2024, *arXiv e-prints*, arXiv:2411.12022, doi: [10.48550/arXiv.2411.12022](https://doi.org/10.48550/arXiv.2411.12022)
- DESI Collaboration, Abdul-Karim, M., Aguilar, J., et al. 2025a, *arXiv e-prints*, arXiv:2503.14738, doi: [10.48550/arXiv.2503.14738](https://doi.org/10.48550/arXiv.2503.14738)

- DESI Collaboration, Abdul-Karim, M., Adame, A. G., et al. 2025b, arXiv e-prints, arXiv:2503.14745, doi: [10.48550/arXiv.2503.14745](https://doi.org/10.48550/arXiv.2503.14745)
- Drake, A. J., Djorgovski, S. G., Mahabal, A., et al. 2009, ApJ, 696, 870, doi: [10.1088/0004-637X/696/1/870](https://doi.org/10.1088/0004-637X/696/1/870)
- Drake, A. J., Catelan, M., Djorgovski, S. G., et al. 2013, ApJ, 763, 32, doi: [10.1088/0004-637X/763/1/32](https://doi.org/10.1088/0004-637X/763/1/32)
- Drake, A. J., Djorgovski, S. G., Catelan, M., et al. 2017, MNRAS, 469, 3688, doi: [10.1093/mnras/stx1085](https://doi.org/10.1093/mnras/stx1085)
- Erkal, D., Li, T. S., Koposov, S. E., et al. 2018, MNRAS, 481, 3148, doi: [10.1093/mnras/sty2518](https://doi.org/10.1093/mnras/sty2518)
- Fabrizio, M., Bono, G., Braga, V. F., et al. 2019, ApJ, 882, 169, doi: [10.3847/1538-4357/ab3977](https://doi.org/10.3847/1538-4357/ab3977)
- Fabrizio, M., Braga, V. F., Crestani, J., et al. 2021, ApJ, 919, 118, doi: [10.3847/1538-4357/ac1115](https://doi.org/10.3847/1538-4357/ac1115)
- Fiorentino, G., Bono, G., Monelli, M., et al. 2015, ApJL, 798, L12, doi: [10.1088/2041-8205/798/1/L12](https://doi.org/10.1088/2041-8205/798/1/L12)
- Fiorentino, G., Monelli, M., Stetson, P. B., et al. 2017, A&A, 599, A125, doi: [10.1051/0004-6361/201629501](https://doi.org/10.1051/0004-6361/201629501)
- Fiorentino, G., Bono, G., Braga, V. F., et al. 2022, in Memorie della Societa Astronomica Italiana, Vol. 93, 47, doi: [10.36116/MEMSAIT\\_93N4.2022.47](https://doi.org/10.36116/MEMSAIT_93N4.2022.47)
- For, B.-Q., & Sneden, C. 2010, AJ, 140, 1694, doi: [10.1088/0004-6256/140/6/1694](https://doi.org/10.1088/0004-6256/140/6/1694)
- For, B.-Q., Sneden, C., & Preston, G. W. 2011, ApJS, 197, 29, doi: [10.1088/0067-0049/197/2/29](https://doi.org/10.1088/0067-0049/197/2/29)
- Foreman-Mackey, D., Hogg, D. W., Lang, D., & Goodman, J. 2013, PASP, 125, 306, doi: [10.1086/670067](https://doi.org/10.1086/670067)
- Gaia Collaboration, Helmi, A., van Leeuwen, F., et al. 2018, A&A, 616, A12, doi: [10.1051/0004-6361/201832698](https://doi.org/10.1051/0004-6361/201832698)
- Garofalo, A., Delgado, H. E., Sarro, L. M., et al. 2022, MNRAS, 513, 788, doi: [10.1093/mnras/stac735](https://doi.org/10.1093/mnras/stac735)
- Gillet, D. 2013, A&A, 554, A46, doi: [10.1051/0004-6361/201220840](https://doi.org/10.1051/0004-6361/201220840)
- Gillet, D., Mauclaire, B., Lemoult, T., et al. 2019, A&A, 623, A109, doi: [10.1051/0004-6361/201833869](https://doi.org/10.1051/0004-6361/201833869)
- GRAVITY Collaboration, Abuter, R., Amorim, A., et al. 2021, A&A, 647, A59, doi: [10.1051/0004-6361/202040208](https://doi.org/10.1051/0004-6361/202040208)
- Guy, J., Bailey, S., Kremin, A., et al. 2023, AJ, 165, 144, doi: [10.3847/1538-3881/acb212](https://doi.org/10.3847/1538-3881/acb212)
- Hajdu, G., Catelan, M., Jurcsik, J., et al. 2015, MNRAS, 449, L113, doi: [10.1093/mnras/slv024](https://doi.org/10.1093/mnras/slv024)
- Hajdu, G., Pietrzyński, G., Jurcsik, J., et al. 2021, ApJ, 915, 50, doi: [10.3847/1538-4357/abff4b](https://doi.org/10.3847/1538-4357/abff4b)
- Hansen, C. J., Nordström, B., Bonifacio, P., et al. 2011, A&A, 527, A65, doi: [10.1051/0004-6361/201015076](https://doi.org/10.1051/0004-6361/201015076)
- Hernquist, L. 1990, ApJ, 356, 359, doi: [10.1086/168845](https://doi.org/10.1086/168845)
- Hunter, J. D. 2007, Computing in Science and Engineering, 9, 90, doi: [10.1109/MCSE.2007.55](https://doi.org/10.1109/MCSE.2007.55)
- Husser, T. O., Wende-von Berg, S., Dreizler, S., et al. 2013, A&A, 553, A6, doi: [10.1051/0004-6361/201219058](https://doi.org/10.1051/0004-6361/201219058)
- Ibata, R., Battaglia, G., Bellazzini, M., et al. 2023, The Messenger, 190, 10, doi: [10.18727/0722-6691/5301](https://doi.org/10.18727/0722-6691/5301)
- Iben, Icko, J. 1971, ApJ, 166, 131, doi: [10.1086/150946](https://doi.org/10.1086/150946)
- Iorio, G., & Belokurov, V. 2021, MNRAS, 502, 5686, doi: [10.1093/mnras/stab005](https://doi.org/10.1093/mnras/stab005)
- Irwin, J. B. 1952, ApJ, 116, 211, doi: [10.1086/145604](https://doi.org/10.1086/145604)
- . 1959, AJ, 64, 149, doi: [10.1086/107913](https://doi.org/10.1086/107913)
- Jayasinghe, T., Kochanek, C. S., Stanek, K. Z., et al. 2018, MNRAS, 477, 3145, doi: [10.1093/mnras/sty838](https://doi.org/10.1093/mnras/sty838)
- Jayasinghe, T., Stanek, K. Z., Kochanek, C. S., et al. 2020, MNRAS, 491, 13, doi: [10.1093/mnras/stz2711](https://doi.org/10.1093/mnras/stz2711)
- Jurcsik, J., & Kovacs, G. 1996, A&A, 312, 111
- Jurcsik, J., Smitola, P., Hajdu, G., et al. 2015, ApJS, 219, 25, doi: [10.1088/0067-0049/219/2/25](https://doi.org/10.1088/0067-0049/219/2/25)
- Karczmarek, P., Wiktorowicz, G., İlkiewicz, K., et al. 2017, MNRAS, 466, 2842, doi: [10.1093/mnras/stw3286](https://doi.org/10.1093/mnras/stw3286)
- Kervella, P., Gallenne, A., Rameau Evans, N., et al. 2019, A&A, 623, A116, doi: [10.1051/0004-6361/201834210](https://doi.org/10.1051/0004-6361/201834210)
- Kim, B., Koposov, S. E., Li, T. S., et al. 2025, arXiv e-prints, arXiv:2504.20327, doi: [10.48550/arXiv.2504.20327](https://doi.org/10.48550/arXiv.2504.20327)
- Koposov, S. E. 2019a, RVSpecFit: Radial velocity and stellar atmospheric parameter fitting, Astrophysics Source Code Library, record ascl:1907.013
- . 2019b, RVSpecFit: Radial velocity and stellar atmospheric parameter fitting. <http://ascl.net/1907.013>
- Koposov, S. E., Belokurov, V., Li, T. S., et al. 2019, MNRAS, 485, 4726, doi: [10.1093/mnras/stz457](https://doi.org/10.1093/mnras/stz457)
- Koposov, S. E., Allende Prieto, C., Cooper, A. P., et al. 2024, MNRAS, 533, 1012, doi: [10.1093/mnras/stae1842](https://doi.org/10.1093/mnras/stae1842)
- Kovács, G., & Walker, A. R. 1999, ApJ, 512, 271, doi: [10.1086/306755](https://doi.org/10.1086/306755)
- Kundu, R., Minniti, D., & Singh, H. P. 2019, MNRAS, 483, 1737, doi: [10.1093/mnras/sty3239](https://doi.org/10.1093/mnras/sty3239)
- Lee, J.-W., & Carney, B. W. 1999, AJ, 118, 1373, doi: [10.1086/301008](https://doi.org/10.1086/301008)
- Levi, M., Bebek, C., Beers, T., et al. 2013, arXiv e-prints, arXiv:1308.0847, doi: [10.48550/arXiv.1308.0847](https://doi.org/10.48550/arXiv.1308.0847)
- Li, L. J., Qian, S. B., Zhu, L. Y., Shi, X. D., & Liao, W. P. 2024, arXiv e-prints, arXiv:2404.00911, doi: [10.48550/arXiv.2404.00911](https://doi.org/10.48550/arXiv.2404.00911)
- Liu, S., Zhao, G., Chen, Y.-Q., Takeda, Y., & Honda, S. 2013, Research in Astronomy and Astrophysics, 13, 1307, doi: [10.1088/1674-4527/13/11/003](https://doi.org/10.1088/1674-4527/13/11/003)
- Liška, J., Skarka, M., Zejda, M., Mikulášek, Z., & de Villiers, S. N. 2016, MNRAS, 459, 4360, doi: [10.1093/mnras/stw851](https://doi.org/10.1093/mnras/stw851)

- Luo, C., Liu, C., Zhang, X., et al. 2021, in *Astronomical Society of the Pacific Conference Series*, Vol. 529, RR Lyrae/Cepheid 2019: Frontiers of Classical Pulsators, ed. K. Kinemuchi, C. Lovekin, H. Neilson, & K. Vivas, 147
- Luongo, E., Ripepi, V., Marconi, M., et al. 2024, arXiv e-prints, arXiv:2409.04259, doi: [10.48550/arXiv.2409.04259](https://doi.org/10.48550/arXiv.2409.04259)
- Majewski, S. R., Schiavon, R. P., Frinchaboy, P. M., et al. 2017, *AJ*, 154, 94, doi: [10.3847/1538-3881/aa784d](https://doi.org/10.3847/1538-3881/aa784d)
- Manser, C. J., Gänsicke, B. T., Inight, K., et al. 2023, *MNRAS*, 521, 4976, doi: [10.1093/mnras/stad727](https://doi.org/10.1093/mnras/stad727)
- Manser, C. J., Izquierdo, P., Gänsicke, B. T., et al. 2024, *MNRAS*, doi: [10.1093/mnras/stae2205](https://doi.org/10.1093/mnras/stae2205)
- Marconi, M., Coppola, G., Bono, G., et al. 2015, *ApJ*, 808, 50, doi: [10.1088/0004-637X/808/1/50](https://doi.org/10.1088/0004-637X/808/1/50)
- Marconi, M., Molinaro, R., Dall’Ora, M., et al. 2022, *ApJ*, 934, 29, doi: [10.3847/1538-4357/ac78ee](https://doi.org/10.3847/1538-4357/ac78ee)
- Marsakov, V. A., Gozha, M. L., & Koval’, V. V. 2019, *Astronomy Reports*, 63, 203, doi: [10.1134/S1063772919020069](https://doi.org/10.1134/S1063772919020069)
- Martínez-Vázquez, C. E., Vivas, A. K., Gurevich, M., et al. 2019, *MNRAS*, 490, 2183, doi: [10.1093/mnras/stz2609](https://doi.org/10.1093/mnras/stz2609)
- Medina, G. E., Hansen, C. J., Muñoz, R. R., et al. 2023, *MNRAS*, 519, 5689, doi: [10.1093/mnras/stac3800](https://doi.org/10.1093/mnras/stac3800)
- Medina, G. E., Muñoz, R. R., Carlin, J. L., et al. 2024, arXiv e-prints, arXiv:2402.14055, doi: [10.48550/arXiv.2402.14055](https://doi.org/10.48550/arXiv.2402.14055)
- Medina, G. E., Muñoz, R. R., Vivas, A. K., et al. 2017, *ApJL*, 845, L10, doi: [10.3847/2041-8213/aa821e](https://doi.org/10.3847/2041-8213/aa821e)
- . 2018, *ApJ*, 855, 43, doi: [10.3847/1538-4357/aaad02](https://doi.org/10.3847/1538-4357/aaad02)
- Medina, G. E., Li, T. S., Kuposov, S. E., et al. 2025, arXiv e-prints, arXiv:2504.02924, doi: [10.48550/arXiv.2504.02924](https://doi.org/10.48550/arXiv.2504.02924)
- Miller, T. N., Doel, P., Gutierrez, G., et al. 2024, *AJ*, 168, 95, doi: [10.3847/1538-3881/ad45fe](https://doi.org/10.3847/1538-3881/ad45fe)
- Miyamoto, M., & Nagai, R. 1975, *PASJ*, 27, 533
- Monelli, M., & Fiorentino, G. 2022, *Universe*, 8, 191, doi: [10.3390/universe8030191](https://doi.org/10.3390/universe8030191)
- Mullen, J. P., Marengo, M., Martínez-Vázquez, C. E., et al. 2021, *ApJ*, 912, 144, doi: [10.3847/1538-4357/abefd4](https://doi.org/10.3847/1538-4357/abefd4)
- . 2022, *ApJ*, 931, 131, doi: [10.3847/1538-4357/ac67ee](https://doi.org/10.3847/1538-4357/ac67ee)
- Muraveva, T., Palmer, M., Clementini, G., et al. 2015, *ApJ*, 807, 127, doi: [10.1088/0004-637X/807/2/127](https://doi.org/10.1088/0004-637X/807/2/127)
- Naidu, R. P., Conroy, C., Bonaca, A., et al. 2020, *ApJ*, 901, 48, doi: [10.3847/1538-4357/abaef4](https://doi.org/10.3847/1538-4357/abaef4)
- Narloch, W., Hajdu, G., Pietrzyński, G., et al. 2024, *A&A*, 689, A138, doi: [10.1051/0004-6361/202450364](https://doi.org/10.1051/0004-6361/202450364)
- Navarrete, C., Contreras Ramos, R., Catelan, M., et al. 2015, *A&A*, 577, A99, doi: [10.1051/0004-6361/201424838](https://doi.org/10.1051/0004-6361/201424838)
- Navarro, J. F., Frenk, C. S., & White, S. D. M. 1997, *ApJ*, 490, 493, doi: [10.1086/304888](https://doi.org/10.1086/304888)
- Neeley, J. R., Marengo, M., Bono, G., et al. 2017, *ApJ*, 841, 84, doi: [10.3847/1538-4357/aa713d](https://doi.org/10.3847/1538-4357/aa713d)
- Nemec, J. M. 1985, *AJ*, 90, 240, doi: [10.1086/113728](https://doi.org/10.1086/113728)
- Nemec, J. M., Cohen, J. G., Ripepi, V., et al. 2013, *ApJ*, 773, 181, doi: [10.1088/0004-637X/773/2/181](https://doi.org/10.1088/0004-637X/773/2/181)
- Nemec, J. M., Linnell Nemec, A. F., Moskalik, P., et al. 2024, *MNRAS*, 529, 296, doi: [10.1093/mnras/stae424](https://doi.org/10.1093/mnras/stae424)
- Netzel, H. 2022, *Video Memorie della Societa Astronomica Italiana*, 2, 22, doi: [10.36116/VIDEOMEM.2.2022.22](https://doi.org/10.36116/VIDEOMEM.2.2022.22)
- Oosterhoff, P. T. 1939, *The Observatory*, 62, 104
- Paxton, B., Bildsten, L., Dotter, A., et al. 2011, *ApJS*, 192, 3, doi: [10.1088/0067-0049/192/1/3](https://doi.org/10.1088/0067-0049/192/1/3)
- Paxton, B., Smolec, R., Schwab, J., et al. 2019, *ApJS*, 243, 10, doi: [10.3847/1538-4365/ab2241](https://doi.org/10.3847/1538-4365/ab2241)
- Petersen, J. O. 1973, *A&A*, 27, 89
- Pietrzyński, G., Graczyk, D., Gellenne, A., et al. 2019, *Nature*, 567, 200, doi: [10.1038/s41586-019-0999-4](https://doi.org/10.1038/s41586-019-0999-4)
- Popielski, B. L., Dziembowski, W. A., & Cassisi, S. 2000, *AcA*, 50, 491, doi: [10.48550/arXiv.astro-ph/0011442](https://doi.org/10.48550/arXiv.astro-ph/0011442)
- Poppett, C., Tyas, L., Aguilar, J., et al. 2024, *AJ*, 168, 245, doi: [10.3847/1538-3881/ad76a4](https://doi.org/10.3847/1538-3881/ad76a4)
- Preston, G. W. 1959, *ApJ*, 130, 507, doi: [10.1086/146743](https://doi.org/10.1086/146743)
- Preston, G. W., Sneden, C., Thompson, I. B., Sheckman, S. A., & Burley, G. S. 2006, *AJ*, 132, 85, doi: [10.1086/504425](https://doi.org/10.1086/504425)
- Prudil, Z., Dékány, I., Grebel, E. K., & Kunder, A. 2020, *MNRAS*, 492, 3408, doi: [10.1093/mnras/staa046](https://doi.org/10.1093/mnras/staa046)
- Prudil, Z., & Ferro, A. A. 2024, *MNRAS*, doi: [10.1093/mnras/stae2335](https://doi.org/10.1093/mnras/stae2335)
- Prudil, Z., Kunder, A., Dékány, I., & Koch-Hansen, A. J. 2024, *A&A*, 684, A176, doi: [10.1051/0004-6361/202347338](https://doi.org/10.1051/0004-6361/202347338)
- Prudil, Z., Skarka, M., Liška, J., Grebel, E. K., & Lee, C. U. 2019, *MNRAS*, 487, L1, doi: [10.1093/mnras/rlz069](https://doi.org/10.1093/mnras/rlz069)
- Sandage, A. 1993, *AJ*, 106, 703, doi: [10.1086/116676](https://doi.org/10.1086/116676)
- Savino, A., Koch, A., Prudil, Z., Kunder, A., & Smolec, R. 2020, *A&A*, 641, A96, doi: [10.1051/0004-6361/202038305](https://doi.org/10.1051/0004-6361/202038305)
- Schatzman, E. 1956, *Annales d’Astrophysique*, 19, 51
- Schlafly, E. F., Kirkby, D., Schlegel, D. J., et al. 2023, *AJ*, 166, 259, doi: [10.3847/1538-3881/ad0832](https://doi.org/10.3847/1538-3881/ad0832)
- Sesar, B., Hernitschek, N., Mitrović, S., et al. 2017, *AJ*, 153, 204, doi: [10.3847/1538-3881/aa661b](https://doi.org/10.3847/1538-3881/aa661b)
- Shipp, N., Erkal, D., Drlica-Wagner, A., et al. 2021, arXiv e-prints, arXiv:2107.13004, <https://arxiv.org/abs/2107.13004>
- Smolec, R. 2005, *AcA*, 55, 59, doi: [10.48550/arXiv.astro-ph/0503614](https://doi.org/10.48550/arXiv.astro-ph/0503614)

- Smolec, R., Pietrzyński, G., Graczyk, D., et al. 2013, MNRAS, 428, 3034, doi: [10.1093/mnras/sts258](https://doi.org/10.1093/mnras/sts258)
- Smolec, R., Soszyński, I., Udalski, A., et al. 2015, MNRAS, 447, 3756, doi: [10.1093/mnras/stu2684](https://doi.org/10.1093/mnras/stu2684)
- Snedden, C., Preston, G. W., Chadid, M., & Adamów, M. 2017, ApJ, 848, 68, doi: [10.3847/1538-4357/aa8b10](https://doi.org/10.3847/1538-4357/aa8b10)
- Soszyński, I., Dziembowski, W. A., Udalski, A., et al. 2011, AcA, 61, 1, doi: [10.48550/arXiv.1105.6126](https://doi.org/10.48550/arXiv.1105.6126)
- Soszyński, I., Udalski, A., Szymański, M. K., et al. 2014, AcA, 64, 177, doi: [10.48550/arXiv.1410.1542](https://doi.org/10.48550/arXiv.1410.1542)
- Soszyński, I., Smolec, R., Dziembowski, W. A., et al. 2016, MNRAS, 463, 1332, doi: [10.1093/mnras/stw1933](https://doi.org/10.1093/mnras/stw1933)
- Soszyński, I., Udalski, A., Wrona, M., et al. 2019, AcA, 69, 321, doi: [10.32023/0001-5237/69.4.2](https://doi.org/10.32023/0001-5237/69.4.2)
- Sterken, C. 2005, in *Astronomical Society of the Pacific Conference Series*, Vol. 335, *The Light-Time Effect in Astrophysics: Causes and cures of the O-C diagram*, ed. C. Sterken, 3
- Stringer, K. M., Drlica-Wagner, A., Macri, L., et al. 2021, ApJ, 911, 109, doi: [10.3847/1538-4357/abe873](https://doi.org/10.3847/1538-4357/abe873)
- Takada, M., Ellis, R. S., Chiba, M., et al. 2014, PASJ, 66, R1, doi: [10.1093/pasj/pst019](https://doi.org/10.1093/pasj/pst019)
- Tamura, N., Takato, N., Shimono, A., et al. 2016, in *Society of Photo-Optical Instrumentation Engineers (SPIE) Conference Series*, Vol. 9908, *Ground-based and Airborne Instrumentation for Astronomy VI*, ed. C. J. Evans, L. Simard, & H. Takami, 99081M, doi: [10.1117/12.2232103](https://doi.org/10.1117/12.2232103)
- Torrealba, G., Catelan, M., Drake, A. J., et al. 2015, MNRAS, 446, 2251, doi: [10.1093/mnras/stu2274](https://doi.org/10.1093/mnras/stu2274)
- Torrealba, G., Belokurov, V., Koposov, S. E., et al. 2019, MNRAS, 488, 2743, doi: [10.1093/mnras/stz1624](https://doi.org/10.1093/mnras/stz1624)
- van Albada, T. S., & Baker, N. 1971, ApJ, 169, 311, doi: [10.1086/151144](https://doi.org/10.1086/151144)
- . 1973, ApJ, 185, 477, doi: [10.1086/152434](https://doi.org/10.1086/152434)
- van der Marel, R. P., Alves, D. R., Hardy, E., & Suntzeff, N. B. 2002, AJ, 124, 2639, doi: [10.1086/343775](https://doi.org/10.1086/343775)
- van der Marel, R. P., & Kallivayalil, N. 2014, ApJ, 781, 121, doi: [10.1088/0004-637X/781/2/121](https://doi.org/10.1088/0004-637X/781/2/121)
- van der Walt, S., Colbert, S. C., & Varoquaux, G. 2011, *Computing in Science and Engineering*, 13, 22, doi: [10.1109/MCSE.2011.37](https://doi.org/10.1109/MCSE.2011.37)
- Varma, V., & Ngeow, C.-C. 2024, AJ, 168, 43, doi: [10.3847/1538-3881/ad5180](https://doi.org/10.3847/1538-3881/ad5180)
- Vasiliev, E., Belokurov, V., & Erkal, D. 2021, MNRAS, 501, 2279, doi: [10.1093/mnras/staa3673](https://doi.org/10.1093/mnras/staa3673)
- Virtanen, P., Gommers, R., Oliphant, T. E., et al. 2020, *Nature Methods*, 17, 261, doi: [10.1038/s41592-019-0686-2](https://doi.org/10.1038/s41592-019-0686-2)
- Vivas, A. K., Martínez-Vázquez, C., & Walker, A. R. 2020, ApJS, 247, 35, doi: [10.3847/1538-4365/ab67c0](https://doi.org/10.3847/1538-4365/ab67c0)
- Wenger, M., Ochsenbein, F., Egret, D., et al. 2000, A&AS, 143, 9, doi: [10.1051/aas:2000332](https://doi.org/10.1051/aas:2000332)
- Xiong, D.-r. 1982, ChA&A, 6, 43, doi: [10.1016/0275-1062\(82\)90063-7](https://doi.org/10.1016/0275-1062(82)90063-7)
- Zhang, H., Iorio, G., Belokurov, V., et al. 2025, arXiv e-prints, arXiv:2504.06720, doi: [10.48550/arXiv.2504.06720](https://doi.org/10.48550/arXiv.2504.06720)
- Zhang, S., Liu, G., Huang, Y., et al. 2023, MNRAS, 525, 5915, doi: [10.1093/mnras/stad2681](https://doi.org/10.1093/mnras/stad2681)
- Zinn, R., Chen, X., Layden, A. C., & Casetti-Dinescu, D. I. 2020, MNRAS, 492, 2161, doi: [10.1093/mnras/stz3580](https://doi.org/10.1093/mnras/stz3580)
- Zinn, R., Horowitz, B., Vivas, A. K., et al. 2014, ApJ, 781, 22, doi: [10.1088/0004-637X/781/1/22](https://doi.org/10.1088/0004-637X/781/1/22)